

In light of the two anonymous reviews, please find below our responses to the raised issues.

First, we would like to gratefully thank the reviewers for their work in reading and reviewing the manuscript. Please know that all the proposed changes have been made to the manuscript.

In response to anonymous referee #1.

We thank the reviewer for this time in reading the manuscript. We have rewritten a large part of the introduction to clarify the scope and the potential application of this work. Now, the phenomena is first described, using terminology more commonly used within the literature. Afterwards, a short description of existing modelling approaches and their shortcomings is provided. Finally, the introduction ends with the objective of the research: development of a new generalized semi-structured mass movement model.

In terms of the nature of the movements, we have clarified that the model implements structured movements (dynamics of a coherent mass), but similarly can (if required, or if the underlying physics indicates it) simulate fragmentation of the material.

We have addressed our usage of the term “debris-flow” in our work. Instead we use “mass movement”, as it more accurately reflects the generalized nature of the equations. Similarly to the work of Pudasaini (2012) and George and Iverson (2014) and Aaron and Hungr (2016), generalized sets of equations which are sometimes referred to as “debris flow” equations allow for simulation of a much wider range of phenomena.

The applicability of the model to granular flow is, when cohesive strength is insignificant, at least as good as the generalized two-phase equations from Pudasaini (2012) which is the predominant underpinning of this work. The influence of the additional work on cohesive strength and fragmentation has been developed with general validity in mind. When fragmentation occurs in the model, further runout reduces to the two-phase equations of Pudasaini automatically. However, full validation of the model to runout of various types of cohesive matrices must be further investigated.

Finally, all specific comments have been addressed based on the reviewer suggestion.

In response to anonymous referee #2.

We thank the reviewer for this time in reading the manuscript. All the specific comments provided by the reviewer have been addressed in the manuscript. The sections have been re-labeled to be consistent and in line with the comments. Also, we have addressed our usage of the term debris-flow in this work. As with reviewer 1, we agree that mass movement (to be more generic) and specifically rock avalanches and landslides are more closely related to the applicability of this work.

References:

Aaron, J., & Hungr, O. (2016). Dynamic simulation of the motion of partially-coherent landslides. *Engineering Geology*, 205, 1-11.

George, D. L., & Iverson, R. M. (2014). A depth-averaged debris-flow model that includes the effects of evolving dilatancy. II. Numerical predictions and experimental tests. *Proceedings of the Royal Society A: Mathematical, Physical and Engineering Sciences*, 470(2170), 20130820.

Pudasaini, S. P. (2012). A general two-phase debris flow model. *Journal of Geophysical Research: Earth Surface*, 117(F3).

# Towards a model for structured mass movements: the OpenLISEM Hazard model 2.0a

Bastian van den Bout<sup>\*1</sup> Theo van Asch<sup>2</sup> Wei Hu<sup>2</sup> Chenxiao X. Tang<sup>3</sup> Olga Mavrouli<sup>1</sup> Victor G. Jetten<sup>1</sup> Cees J. van Westen<sup>1</sup>

<sup>1</sup>University of Twente, Faculty of Geo-Information Science and Earth Observation

<sup>2</sup>Chengdu university of Technology, State key Laboratory of Geohazard Prevention and GeoEnvironment Protection

<sup>3</sup>Institute of Mountain Hazards and Environment, Chinese Academy of Sciences

*Correspondence to:* Bastian van den Bout (b.vandenbout@utwente.nl)

## Abstract

Mass movements such as debris flows and landslides differ in behavior due to their material properties and internal forces. Models employ generalized multi-phase flow equations to adaptively describe these complex flow types. ~~Such models commonly assume unstructured and fragmented flow, where internal cohesive strength is insignificant. However, models commonly assume unstructured and fragmented flow after initiation of movement.~~ In this work, existing work on two-phase mass movement equations are extended to include a full stress-strain relationship that allows for runoff of (semi-) structured fluid-solid masses. The work provides both the three-dimensional equations and depth-averaged simplifications. The equations are implemented in a hybrid Material Point Method (MPM) which allows for efficient simulation of stress-strain relationships on discrete smooth particles. Using this framework, the developed model is compared to several flume experiments of clay blocks impacting fixed obstacles. Here, both final deposit patterns and fractures compare well to simulations. Additionally, numerical tests are performed to showcase the range of dynamical behavior produced by the model. Important processes such as fracturing, fragmentation and fluid release are captured by the model. While this provides an important step towards complete mass movement models, several new opportunities arise such as ~~ground water flow descriptions and application to fragmenting mass movements and block-slides and block-slides.~~

28 **1. Introduction**

29 The earths rock cycle involves sudden release and gravity-driven transport of sloping materials. These  
30 mass movements have a significant global impact in financial damage and casualties (Nadim et al., 2006;  
31 Kjekstad & Highland, 2009). Understanding the physical principles at work at their initiation and runout phase  
32 allows for better mitigation and adaptation to the hazard they induce (Corominas et al., 2014). Many varieties of  
33 gravitationally-driven mass movements have been categorized according to their material physical parameters  
34 and type of movement. Examples are slides, flows and falls consisting of soil, rocks or debris (Varnes, 1987).  
35 Major factors in determining the dynamics of mass movement runout are the composition of the moving material  
36 and the internal and external forces during initiation and runout.

37 Within the cluster of existing mass movement processes, a distinction can be made based on the  
38 cohesive of the mass during movement. Post-release, a sloping mass might be unstructured, such as mud flows,  
39 where grain-grain cohesive strength is absent. Alternatively, the mass can be fragmentative, such as strongly-  
40 deforming landslides or fragmenting of rock avalanches upon particle impacts. Finally, there are  
41 coherent/structured mass movements, such as can be the case in block-slides where internal cohesive strength  
42 can resist deformation for some period (Varnes, 1987). The general importance of the initially structured nature  
43 of mass movement material is observed for a variety of reasons. First, block slides are an important subset of  
44 mass movement types (Hayir, 2003; Beutner et al., 2008; Tang et al., 2008). This type of mass movement  
45 features some cohesive structure to the dynamic material in the movement phase. Secondly, during movement,  
46 the spatial gradients in local acceleration induce strain and stress that results in fracturing. This process, often  
47 called fragmentation in relation to structured mass movements, can be of crucial importance for mass movement  
48 dynamics (Davies & McSaveney, 2009; Delaney & Evans, 2014; Dufresne et al., 2018; Corominas et al. 2019).  
49 Lubricating effect from basal fragmentation can enhance velocities and runout distance significantly (Davies et  
50 al., 2006; Tang et al., 2009). Otherwise, fragmentation generally influences the rheology of the movement by  
51 altering grain-grain interactions (Zhou et al., 2005). The importance of structured material dynamics is further  
52 indicated by engineering studies on rock behavior and fracture models (Kaklauskas & Ghaboussi, 2001; Ngekke  
53 et al., 2016; Dhanmeher, 2017).

54 Dynamics of geophysical flows are complex and depend on a variety of forces due to their multi-phase  
55 interactions (Hutter et al., 1996). Physically-based models attempt to describe the internal and external forces of  
56 all these mass movements in a generalized form (David & Richard, 2011; Pudasaini, 2012; Iverson & George,  
57 2014). This allows these models to be applied to a wide variety of cases, while improving predictive range.  
58 Generally, understanding and prediction of geophysical flows takes place through numerical modelling of the  
59 flow. A variety of both one, two and three- dimensional sets of equations exist to describe the advection and  
60 forces that determine the dynamics of geophysical flows. A major assumption made for current models is the a  
61 fully mixed and fragmented nature of the material (Iverson & Denlinger 2001; Pudasaini & Hutter, 2003).  
62 Physically-based models attempt to describe the internal and external forces of all these mass movements in a  
63 generalized form (David & Richard, 2011; Pudasaini, 2012; Iverson & George, 2014). This allows these models  
64 to be applied to a wide variety of cases, while improving predictive range.

65  
66 For unstructured (fully fragmented) mass movements, a variety of models exist relating to mohr-  
67 coulomb mixture theory. Dynamics of geophysical flows are complex and depend on a variety of forces due to  
68 their multi-phase interactions (Hutter et al., 1996). Generally, understanding and prediction of geophysical flows  
69 takes place through numerical modelling of the flow. A variety of both one, two and three- dimensional sets of  
70 equations exist to describe the advection and forces that determine the dynamics of geophysical flows. Examples  
71 that simulated a single mixed material (Rickenmann et al., 2006; O'Brien et al., 2007; Luna et al., 2012; van  
72 Asch et al., 2014). Two phase models describe both solids, fluids and their interactions and provide additional  
73 detail and generalize in important ways (Sheridan et al., 2005; Pitman & Le, 2005; Pudasaini, 2012; George &  
74 Iverson, 2014; Mergili et al., 2017). Recently, a three-phase model has been developed that includes the  
75 interactions between small and larger solid phases (Pudasaini & Mergili, 2019). Typically, implemented forces  
76 include gravitational forces and, depending on the rheology of the equations, drag forces, viscous internal forces  
77 and a plasticity-criterion.

78 A major assumption made for current models is the a fully mixed and fragmented nature of the material  
79 (Iverson & Denlinger 2001; Pudasaini & Hutter, 2003). This assumption of unstructured flow is invalid for any  
80 structured mass movement. Some models do implement a non-Newtonian viscous yield stress based on depth-  
81 averaged strain estimations (Boetticher et al., 2016; Fornes et al., 2017; Pudasaini & Mergili, 2019). However,  
82 this approach lacks the process of fragmentation and internal failure.

83 For structured mass movements, with particle-particle cohesive strength, limited approaches are  
84 available. Aaron & Hungr developed a model for simulation of initially coherent rock avalanches (Aaron &

Formatted: Font: (Default) Times New Roman, 10 pt, Bold

Formatted: List Paragraph, Outline numbered + Level: 1 + Numbering Style: 1, 2, 3, ... + Start at: 1 + Alignment: Left + Aligned at: 0.63 cm + Indent at: 1.27

Formatted: Indent: First line: 1.25 cm

85 Hungr, 2016) as part of DAN3D Flex. Within their approach, a rigid-block momentum analysis is used to  
86 simulate initial movement of the block. After a specified time, the block is assumed to fragment, and a granular  
87 flow model using a Voellmy-type rheology is used for further runout. Their approach thus lacks a physical basis  
88 for the fragmenting behavior. Additionally, by dissecting the runout process in two stages (discrete block and  
89 granular flow), benefits of holistic two-phase generalized runout models are lost. Finally, Greco et al. (2019)  
90 presented a runout model for cohesive granular matrix. Their approach similarly lacks a description of the  
91 fragmentation process. Observations of mass movement types indicate that mixing and fracturing is not a  
92 necessary process (Varnes, 1987). Instead, block or slide movement can retain structure during their dynamic  
93 stage, as the material is able to resist the internal deformation stresses. Some models do a non-Newtonian  
94 viscous yield stress based on depth-averaged strain estimations (Boettcher et al., 2016; Fornes et al., 2017;  
95 Pudasaini & Mergili, 2019). However, this approach lacks the process of fragmentation and internal failure.  
96 Thus, within current mass movement models, there might be improvements available from assuming non-  
97 fragmented movement. This would allow for description of structured mass movement dynamics.

98 The general importance of the initially structured nature of mass movement material is observed for a  
99 variety of reasons. First, block slides are an important subset of mass movement types (Hayir, 2003; Beutner et  
100 al., 2008; Tang et al., 2008). This type of mass movement features some cohesive structure to the dynamic  
101 material in the movement phase. Secondly, during movement, the spatial gradients in local acceleration induce  
102 strain and stress that results in fracturing. This process, often called fragmentation in relation to structured mass  
103 movements, can be of crucial importance for mass movement dynamics (Davies & McSaveney, 2009; Delaney  
104 & Evans, 2014; Dufresne et al., 2018; Corominas et al. 2019). Lubricating effect from basal fragmentation can  
105 enhance velocities and runout distance significantly (Davies et al., 2006; Tang et al., 2009). Otherwise,  
106 fragmentation generally influences the rheology of the movement by altering grain-grain interactions (Zhou et  
107 al., 2005). The importance of structured material dynamics is further indicated by engineering studies on rock  
108 behavior and fracture models (Kaklauskas & Ghaboussi, 2001; Ngekpe et al., 2016; Dhanmeher, 2017)

109 In this paper, a generalized mass movement model existing two-phase generalized debris flow equations  
110 are adapted is developed to describe runout of an arbitrarily structured two-phase Mohr-Coulomb material. The  
111 model extends on recent innovations in generalized models for mohr-coulomb mixture flow (Pudasaini, 2012;  
112 Pudasaini & Mergili, 2019). The second section of this work provides the derivation of the extensive set of  
113 equations that describe structured mass movements in a generalized manner. The third section validates the  
114 developed model by comparison with results from controlled flume runout experiments. Additionally, this  
115 section shows numerical simulation examples that highlight fragmentation behavior and its influence on runout  
116 dynamics. Finally, in section four, a discussion on the potential usage of the presented model is provided  
117 together with reflection on important opportunities of improvement.

## 118 4-2. A set of debris flow mass movement equations incorporating internal structure

### 119 2.14.4 Structured mass movements

120 Initiation of gravitational mass flows occurs when sloping material is released. The instability of such  
121 materials is generally understood to take place along a failure plane (Zhang et al., 2011, Stead & Wolter, 2015).  
122 Along this plane, forces exerted due to gravity and possible seismic accelerations can act as a driving force  
123 towards the downslope direction, while a normal-force on the terrain induces a resisting force (Xie et al., 2006).  
124 When internal stress exceeds a specified criteria, commonly described using Mohr-Coulomb theory, fracturing  
125 occurs, and the material becomes dynamic. Observations indicate material can initially fracture predominantly at  
126 the failure plane (Tang et al., 2009; Davies et al., 2006). Full finite-element modelling of stability confirms no  
127 fragmentation occurs at initiation, and runout can start as a structured mass (Matsui & San, 1992; Griffiths &  
128 Lane, 1999).

129 Once movement is initiated, the material is accelerated. Due to spatially non-homogeneous acceleration,  
130 either caused by a non-homogeneous terrain slope, or impact with obstacles, internal stress can build within the  
131 moving mass. The stress state can reach a point outside the yield surface, after which some form of deformation  
132 occurs (e.g. Plastic, Brittle, ductile) (Loehner et al., 2008). In the case of rock or soil material, elastic/plastic  
133 deformation is limited and fracturing occurs at relatively low strain values (Kaklauskas & Ghaboussi, 2001;  
134 Dhanmeher., 2017). Rocks and soil additionally show predominantly brittle fracturing, where strain increments  
135 at maximum stress are small (Bieniawski, 1967; Price, 2016; Husek et al., 2016). For soil matrices, cohesive  
136 bonds between grains originate from causes such as cementing, frictional contacts and root networks (Cohen et  
137 al., 2009). Thus, the material breaks along either the grain-grain bonds or on the molecular level. In practice, this  
138 processes of fragmentation has been both observed and studied frequently. Cracking models for solids use stress-  
139 strain descriptions of continuum mechanics (Menin et al., 2009; Ngekpe et al., 2016). Fracture models frequently  
140 use Smooth Particle Hydrodynamics (SPH) since a Lagrangian, meshfree solution benefits possible fracturing  
141 behavior (Maurel & Combescure, 2008; Xu et al., 2010; Osorno & Steeb, 2017). Within the model developed

Formatted: Font: (Default) Times New Roman, 10 pt, Bold

Formatted: Outline numbered + Level: 1 + Numbering Style: 1, 2, 3, ... + Start at: 1 + Alignment: Left + Aligned at: 0.63 cm + Indent at: 1.27 cm

142 below, knowledge from fracture-simulating continuum mechanical models is combined with finite element fluid  
143 dynamic models.

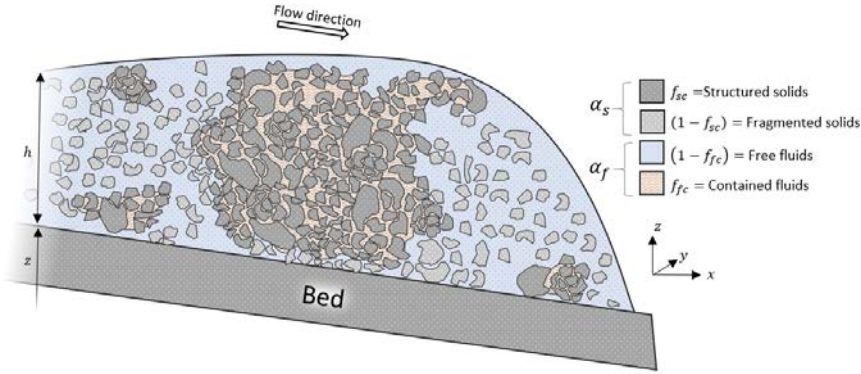
144 The mohr-coulomb mixture models on which the developed model is based, can be found in Pitman &  
145 Le (2005), Pudasaini (2012), George & Iverson, 2014 and Pudasaini & Mergili (2019). While these are  
146 commonly names debris-flow models, their validity extends beyond this typical category of mass movement.  
147 This is both apparent from model applications (Mergili et al., 2018) and theoretical considerations (Pudasaini,  
148 2012). A major cause for the usage of debris flow as a term here is the assumption of unstructured flow, which  
149 we are aiming to solve in this work.

## 150 **2.1.2 Model description**

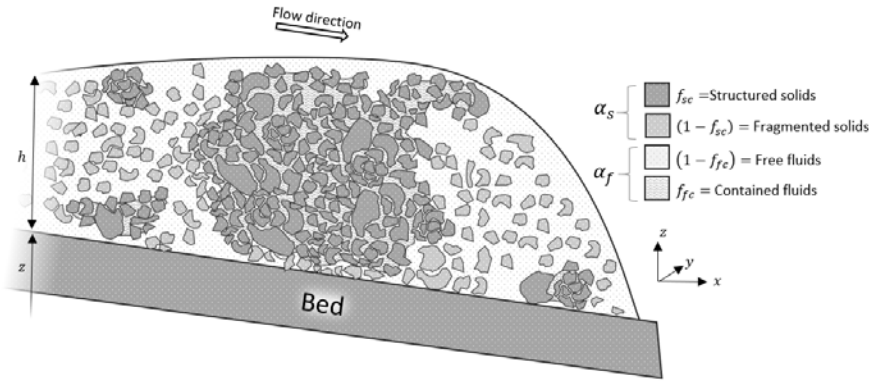
151 We define two phases, solids and fluids, within the flow, indicated by  $s$  and  $f$  respectively. A specified  
152 fraction of solids within this mixture is at any point part of a structured matrix. This structured solid phase,  
153 indicated by  $sc$  envelops and confines a fraction of the fluids in the mixture, indicates as  $fc$ . The solids and  
154 fluids are defined in terms of the physical properties such as densities ( $\rho_f, \rho_s$ ) and volume fractions ( $\alpha_f =$   
155  $\frac{sf}{f+s}, \alpha_s = \frac{fs}{f+s}$ ). The confined fractions of their respective phases are indicated as  $f_{sc}$  and  $f_{fc}$  for the volume  
156 fraction of confined solids and fluids respectively (Equations 1,2 and 3).

- 157 1.  $\alpha_s + \alpha_f = 1$
- 158 2.  $\alpha_s(f_{sc} + (1 - f_{sc})) + \alpha_f(f_{fc} + (1 - f_{fc})) = 1$
- 159 3.  $(f_{sc} + (1 - f_{sc})) = (f_{fc} + (1 - f_{fc})) = 1$

160 For the solids, additionally internal friction angle ( $\phi_s$ ) and effective (volume-averaged) material size  
161 ( $d_s$ ) are defined. We additionally define  $\alpha_c = \alpha_s + f_{fc}\alpha_f$  and  $\alpha_u = (1 - f_{fc})\alpha_f$  to indicate the solids with  
162 confined fluids and free fluid phases respectively. These phases have a volume-averaged density  $\rho_{sc}, \rho_f$ . We let  
163 the velocities of the unconfined fluid phase ( $\alpha_u = (1 - f_{fc})\alpha_f$ ) be defined as  $u_u = (u_u, v_u)$ . We assume  
164 velocities of the confined phases ( $\alpha_c = \alpha_s + f_{fc}\alpha_f$ ) can validly be assumed to be identical to the velocities of  
165 the solid phase,  $u_c = (u_c, v_c) = u_s = (u_s, v_s)$ . A schematic depiction of the represented phases is shown in  
166 Figure 1.



167



168

169 *Figure 1 A schematic depiction of the flow contents. Both structured and unstructured solids are*  
 170 *present. Fluids can be either free, or confined by the structured solids.*

171 A major assumption is made here concerning the velocities of both the confined and free solids (sc and  
 172 s), that have a shared averaged velocity ( $u_s$ ). We deliberately limit the flow description to two phases, opposed  
 173 to the innovative work of Pudasaini & Mergili (2019) that develop a multi-mechanical three-phase model. This  
 174 choice is motivated by considerations of applicability (reducing the number of required parameters), the infancy  
 175 of three-phase flow descriptions and finally the general observations of the validity of this assumption (Ishii,  
 176 1975; Ishii & Zuber, 1979; Drew, 1983; Jakob et al, 2005; George & Iverson, 2016).

177 The movement of the flow is described initially by means of mass and momentum conservation  
 178 (Equations 4 and 5).

179 4.  $\frac{\partial \alpha_c}{\partial t} + \nabla \cdot (\alpha_c \mathbf{u}_c) = 0$

180 5.  $\frac{\partial \alpha_u}{\partial t} + \nabla \cdot (\alpha_u \mathbf{u}_u) = 0$

181 Here we add the individual forces based on the work of Pudasaini & Hutter (2003), Pitman & Le  
 182 (2005), Pudasaini (2012), Pudasaini & Fischer (2016) and Pudasaini & Mergili (2019) (Equations 6 and 7).

183 6.  $\frac{\partial}{\partial t} (\alpha_c \rho_c \mathbf{u}_c) + \nabla \cdot (\alpha_c \rho_c \mathbf{u}_c \otimes \mathbf{u}_c) = \alpha_c \rho_c \mathbf{f} - \nabla \cdot \alpha_c \mathbf{T}_c + p_c \nabla \alpha_c + \mathbf{M}_{DG} + \mathbf{M}_{vm}$

184 7.  $\frac{\partial}{\partial t} (\alpha_u \rho_f \mathbf{u}_u) + \nabla \cdot (\alpha_u \rho_f \mathbf{u}_u \otimes \mathbf{u}_u) = \alpha_u \rho_f \mathbf{f} - \nabla \cdot \alpha_u \mathbf{T}_u + p_f \nabla \alpha_u - \mathbf{M}_{DG} - \mathbf{M}_{vm}$

185 Where  $\mathbf{f}$  is the body force (among which is gravity),  $\mathbf{M}_{DG}$  is the drag force,  $\mathbf{M}_{vm}$  is the virtual mass  
 186 force and  $\mathbf{T}_c, \mathbf{T}_u$  are the stress tensors for solids with confined fluids and unconfined phases respectively. The  
 187 virtual mass force described the additional work required by differential acceleration of the phases. The drag

188 force describes the drag along the interfacial boundary of fluids and solids. The body force describes external  
 189 forces such as gravitational acceleration and boundary forces. Finally, the stress tensors describe the internal  
 190 forces arising from strain and viscous processes. Both the confined and unconfined phases in the mixture are  
 191 subject to stress tensors ( $T_c$ , and  $T_u$ ), for which the gradient acts as a momentum source. Additionally, we follow  
 192 Pudasaini (2012) and add a buoyancy force ( $p_c \nabla \alpha_c$  and  $p_f \nabla \alpha_u$ ).

### 193 Stress Tensors, Describing internal structure

194 Based on known two-phase mixture theory, the internal and external forces acting on the moving  
 195 material are now set up. This results in several unknowns such as the stress tensors ( $T_c$  and  $T_u$ , described by the  
 196 constitutive equation), the body force ( $f$ ), the drag force ( $M_{DG}$ ) and the virtual mass force ( $M_{VM}$ ). This section  
 197 will first describe the derivation of the stress tensors. These describe the internal stress and viscous effects. To  
 198 describe structured movements, these require a full stress-strain relationship which is not present in earlier  
 199 generalized mass movements model. Afterwards, existing derivation of the body, drag and virtual mass force are  
 200 altered to conform to the new constitutive equation.

201 Our first step in defining the momentum source terms in equations 6 and 7 is the definition of the fluid  
 202 and solid stress tensors. Current models typically follow the assumptions made by Pitman & Le (2005), who  
 203 indicate: “Proportionality and alignment of the tangential and normal forces are imposed as a basal boundary  
 204 condition is assumed to hold throughout the layer of flowing material ... following Rankine (1857) and Terzaghi  
 205 (1936), an earth pressure relation is assumed for diagonal stress components”. Here, the earth pressure  
 206 relationship is a vertically-averaged analytical solution for lateral forces exerted by an earth wall. Thus,  
 207 unstructured columns of moving mixtures are assumed. Here, we aim to use the full Mohr-Coulomb relations.  
 208 Describing the internal stress of soil and rock matrices is commonly achieved by elastic-plastic simulations of  
 209 the materials stress-strain relationship. Since we aim to model a full stress description, the stress tensor is equal  
 210 to the elasto-plastic stress tensor (Equation 8).

$$211 \quad 8. \quad T_c = \sigma$$

212 Where  $\sigma$  is the elasto-plastic stress tensor for solids. The stress can be divided into the deviatoric and  
 213 non-deviatoric contributions (Equation 9). The non-deviatoric part acts normal on any plane element (in the  
 214 manner in which a hydrostatic pressure acts equal in all directions). Note that we switch to tensor notation when  
 215 describing the stress-strain relationship. Thus, superscripts ( $\alpha$  and  $\beta$ ) represent the indices of basis vectors (x, y  
 216 or z axis in Euclidian space), and obtain tensor elements. Additionally, the Einstein convention is followed  
 217 (automatic summation of non-defined repeated indices in a single term).

$$218 \quad 9. \quad \sigma^{\alpha\beta} = s^{\alpha\beta} + \frac{1}{3} \sigma^{\gamma\gamma} \delta^{\alpha\beta}$$

219 Where  $s$  is the deviatoric stress tensor and  $\delta^{\alpha\beta} = [\alpha = \beta]$  is the Kronecker delta.

220 Here, we define the elasto-plastic stress ( $\sigma$ ) based on a generalized Hooke-type law in tensor notation  
 221 (Equation 10 and 11) where plastic strain occurs when the stress state reaches the yield criterion (Spencer, 2004;  
 222 Necas & Hlavecek, 2007; Bui et al., 2008).

$$223 \quad 10. \quad \dot{\epsilon}_{elastic}^{\alpha\beta} = \frac{\dot{s}^{\alpha\beta}}{2G} + \frac{1-2\nu}{E} \dot{\sigma}^m \delta^{\alpha\beta}$$

$$224 \quad 11. \quad \dot{\epsilon}_{plastic}^{\alpha\beta} = \dot{\lambda} \frac{\partial g}{\partial \sigma^{\alpha\beta}}$$

225 Where  $\dot{\epsilon}_{elastic}$  is the elastic strain tensor,  $\dot{\epsilon}_{plastic}$  is the plastic strain tensor,  $\dot{\sigma}^m$  is the mean stress rate  
 226 tensor,  $\nu$  is Poisson's ratio,  $E$  is the elastic Young's Modulus,  $G$  is the shear modulus,  $\dot{s}$  is the deviatoric shear  
 227 stress rate tensor,  $\dot{\lambda}$  is the plastic multiplier rate and  $g$  is the plastic potential function. Additionally, the strain  
 228 rate is defined from velocity gradients as equation 12.

$$229 \quad 12. \quad \dot{\epsilon}_{total}^{\alpha\beta} = \dot{\epsilon}_{elastic}^{\alpha\beta} + \dot{\epsilon}_{plastic}^{\alpha\beta} = \frac{1}{2} \left( \frac{\partial u_c^\alpha}{\partial x^\beta} - \frac{\partial u_c^\beta}{\partial x^\alpha} \right)$$

230 By solving equations 9, 10 and 11 for  $\dot{\sigma}$ , a stress-strain relationship can be obtained (Equation 13) (Bui  
 231 et al., 2008).

$$232 \quad 13. \quad \dot{\sigma}^{\alpha\beta} = 2G \dot{\epsilon}^{\gamma\gamma} \delta^{\alpha\beta} + K \dot{\epsilon}^{\gamma\gamma} \delta^{\alpha\beta} - \dot{\lambda} \left[ \left( K - \frac{2G}{3} \right) \frac{\partial g}{\partial \sigma^{mn}} \delta^{mn} \delta^{\alpha\beta} + 2G \frac{\partial g}{\partial \sigma^{\alpha\beta}} \right]$$

233 Where  $\dot{\epsilon}$  is the deviatoric strain rate ( $\dot{\epsilon}^{\alpha\beta} = \dot{\epsilon}^{\gamma\gamma} - \frac{1}{3} \dot{\epsilon}^{\alpha\beta} \delta^{\alpha\beta}$ ),  $\psi$  is the dilatancy angle and  $K$  is the  
 234 elastic bulk modulus and the material parameters defined from  $E$  and  $\nu$  (Equation 14).

$$235 \quad 14. \quad K = \frac{E}{3(1-2\nu)}, \quad G = \frac{E}{2(1+\nu)}$$

236 Fracturing or failure occurs when the stress state reaches the yield surface, after which plastic  
 237 deformation occurs. The rate of change of the plastic multiplier specifies the magnitude of plastic loading and  
 238 must ensure a new stress state conforms to the conditions of the yield criterion. By means of substituting  
 239 equation 13 in the consistency condition ( $\frac{\partial f}{\partial \sigma^{\alpha\beta}} d\sigma^{\alpha\beta} = 0$ ), the plastic multiplier rate can be defined (Equation  
 240 15) (Bui et al., 2008).

$$241 \quad 15. \quad \dot{\lambda} = \frac{2G\epsilon^{\alpha\beta} \frac{\partial f}{\partial \sigma^{\alpha\beta}} + (K - \frac{2G}{3}) \epsilon^{\gamma\gamma} \frac{\partial f}{\partial \sigma^{\alpha\beta}} \sigma^{\alpha\beta} \delta^{\alpha\beta}}{2G \frac{\partial f}{\partial \sigma^{mn}} \frac{\partial g}{\partial \sigma^{mn}} + (K - \frac{2G}{3}) \frac{\partial f}{\partial \sigma^{mn}} \delta^{mn} \frac{\partial g}{\partial \sigma^{mn}} \delta^{mn}}$$

242 The yield criteria specifies a surface in the stress-state space that the stress state can not pass, and at  
 243 which plastic deformation occurs. A variety of yield criteria exist, such as Mohr-Coulomb, Von Mises, Ducker-  
 244 Prager and Tresca (Spencer, 2004). Here, we employ the Ducker-Prager model fitted to Mohr-Coulomb material  
 245 parameters for its accuracy in simulating rock and soil behavior, and numerical stability (Spencer, 2004; Bui et  
 246 al., 2008) (Equation 16 and 17).

$$247 \quad 16. \quad f(I_1, J_2) = \sqrt{J_2} + \alpha_\phi I_1 - k_c = 0$$

$$248 \quad 17. \quad g(I_1, J_2) = \sqrt{J_2} + \alpha_\phi I_1 \sin(\psi)$$

249 Where  $I_1$  and  $J_2$  are tensor invariants (Equation 18 and 19).

$$250 \quad 18. \quad I_1 = \sigma^{xx} + \sigma^{yy} + \sigma^{zz}$$

$$251 \quad 19. \quad J_2 = \frac{1}{2} s^{\alpha\beta} s^{\alpha\beta}$$

252 Where the Mohr-Coulomb material parameters are used to estimate the Ducker-Prager parameters  
 253 (Equation 20).

$$254 \quad 20. \quad \alpha_\phi = \frac{\tan(\phi)}{\sqrt{9+12 \tan^2 \phi}}, \quad k_c = \frac{3c}{\sqrt{9+12 \tan^2 \phi}}$$

255 Using the definitions of the yield surface and stress-strain relationship, combining equations 13, 15, 16  
 256 and 17, the relationship for the stress rate can be obtained (Equation 21 and 22).

$$257 \quad 21. \quad \dot{\sigma} = 2G \dot{\epsilon}^{\alpha\beta} + K \dot{\epsilon}^{\gamma\gamma} \delta^{\alpha\beta} - \dot{\lambda} \left[ 9K \sin\psi \delta^{\alpha\beta} + \frac{G}{\sqrt{J_2}} s^{\alpha\beta} \right]$$

$$258 \quad 22. \quad \dot{\lambda} = \frac{3\alpha K \epsilon^{\gamma\gamma} + \left(\frac{G}{\sqrt{J_2}}\right) s^{\alpha\beta} \dot{\epsilon}^{\alpha\beta}}{27\alpha_\phi K \sin\psi + G}$$

259 In order to allow for the description of large deformation, the Joumann stress rate can be used, which is  
 260 a stress-rate that is independent from a frame of reference (Equation 23).

$$261 \quad 23. \quad \hat{\sigma} = \sigma^{\alpha\gamma} \dot{\omega}^{\beta\gamma} + \sigma^{\gamma\beta} \dot{\omega}^{\alpha\gamma} + 2G \dot{\epsilon}^{\alpha\beta} + K \dot{\epsilon}^{\gamma\gamma} \delta^{\alpha\beta} - \dot{\lambda} \left[ 9K \sin\psi \delta^{\alpha\beta} + \frac{G}{\sqrt{J_2}} s^{\alpha\beta} \right]$$

262 Where  $\dot{\omega}$  is the spin rate tensor, as defined by equation 24.

$$263 \quad 24. \quad \dot{\omega}^{\alpha\beta} = \frac{1}{2} \left( \frac{\partial v^\alpha}{\partial x^\beta} - \frac{\partial v^\beta}{\partial x^\alpha} \right)$$

264 Due to the strain within the confined material, the density of the confined solid phase ( $\rho_c$ ) evolves  
 265 dynamically according to equation 25.

$$266 \quad 25. \quad \rho_c = f_{sc} \rho_s \frac{\epsilon_v}{\epsilon_v} + (1 - f_{sc}) \rho_s + f_{fc} \rho_f$$

267 Where  $\epsilon_v$  is the total volume strain,  $\epsilon_v \approx \epsilon_1 + \epsilon_2 + \epsilon_3$ ,  $\epsilon_i$  is one of the principal components of the  
 268 strain tensor. Since we aim to simulate brittle materials, where volume strain remains relatively low, we assume  
 269 that changes in density are small compared to the original density of the material ( $\frac{\partial \rho_c}{\partial t} \ll \rho_c$ ).

## 270 Fragmentation

271 Brittle fracturing is a processes commonly understood to take place once a material internal stress has  
 272 reached the yield surface, and plastic deformation has been sufficient to pass the ultimate strength point (Maurel  
 273 & Cumescore, 2008; Husek et al., 2016). A variety of approaches to fracturing exist within the literature (Ma et  
 274 al., 2014; Osomo & Steeb, 2017). FEM models use strain-based approaches (Loehnert et al., 2008). For SPH  
 275 implementations, as will be presented in this work, distance-based approaches have provided good results  
 276 (Maurel & Cumescore, 2008). Other works have used strain-based fracture criteria (Xu et al., 2010).  
 277 Additionally, dynamic degradation of strength parameters have been implemented (Grady & Kipp, 1980; Vuyst



278 & Vignjevic, 2013; Williams, 2019). Comparisons with observed fracture behavior has indicated the predictive  
 279 value of these schemes (Xu et al., 2010; Husek et al., 2016). We combine the various approaches to best fit the  
 280 dynamical multi-phase mass movement model that is developed. Following, Grady & Kipp (1980) and we  
 281 simulate a degradation of strength parameters. Our material consists of a soil and rock matrix. We assume  
 282 fracturing occurs along the inter-granular or inter-rock contacts and bonds (see also Cohen et al., 2009). Thus,  
 283 cohesive strength is lost for any fractured contacts. We simulate degradation of cohesive strength according to a  
 284 volume strain criteria. When the stress state lies on the yield surface (the set of critical stress states within the 6-  
 285 dimensional stress-space), during plastic deformation, strain is assumed to attribute towards fracturing. A critical  
 286 volume strain is taken as material property, and the breaking of cohesive bonds occurs based on the relative  
 287 volume strain. Following Grady & Kipp (1980) and Vuyst & Vignjevic (2013), we assume that the degradation  
 288 behavior of the strength parameter is distributed according to a probability density distribution. Commonly, a  
 289 Weibull-distribution is used (Williams, 2019). Here, for simplicity, we use a uniform distribution of cohesive  
 290 strength between 0 and  $2c_0$ , although any other distribution can be substituted. Thus, the expression governing  
 291 cohesive strength becomes equation 26

$$26. \frac{\partial c}{\partial t} = \begin{cases} -c_0 \frac{1}{2} \frac{(\frac{\epsilon_v}{\epsilon_{v0}})}{\epsilon_c} & f(I_1, J_2) \geq 0, c > 0 \\ 0 & otherwise \end{cases}$$

293 Where  $c_0$  is the initial cohesive strength of the material,  $\epsilon_{v0}$  is the initial volume,  $(\frac{\epsilon_v}{\epsilon_{v0}})$  is the fractional  
 294 volumetric strain rate,  $\epsilon_c$  is the critical fractional volume strain for fracturing.

#### 295 **-Water partitioning**

296 During the movement of the mixed mass, the solids can thus be present as a structured matrix. Within  
 297 such a matrix, a fluid volume can be contained (e.g. as originating from a ground water content in the original  
 298 landslide material). These fluids are typically described as groundwater flow following Darcy's law, which poses  
 299 a linear relationship between pressure gradients and flow velocity through a soil matrix. In our case, we assumed  
 300 the relative velocity of water flow within the granular solid matrix as very small compared to both solid  
 301 velocities and the velocities of the free fluids. As an initial condition of the material, some fraction of the water  
 302 is contained within the soil matrix ( $f_{fc}$ ). Additionally, for loss of cohesive structure within the solid phase, we  
 303 transfer the related fraction of fluids contained within that solid structure to the free fluids.

$$304 \quad 27. \frac{\partial f_{fc}}{\partial t} = -\frac{\partial(1-f_{fc})}{\partial t} = \begin{cases} -f_{fc} \frac{c_0 \max(0.0, \epsilon_v)}{c \epsilon_f} & f(I_1, J_2) \geq 0, c > 0 \\ 0 & otherwise \end{cases}$$

$$305 \quad 28. \frac{\partial f_{sc}}{\partial t} = -\frac{\partial(1-f_{sc})}{\partial t} = \begin{cases} -f_{sc} \frac{c_0 \max(0.0, \epsilon_v)}{c \epsilon_f} & f(I_1, J_2) \geq 0, c > 0 \\ 0 & otherwise \end{cases}$$

306 Beyond changes in  $f_{fc}$  through fracturing of structured solid materials, no dynamics are simulated for  
 307 in- or outflux of fluids from the solid-matrix. The initial volume fraction of fluids in the solid matrix defined by  
 308 ( $f_{fc}$  and  $s f_{sc}$ ) remains constant throughout the simulation. The validity of this assumption can be based on the  
 309 slow typical fluid velocities in a solid matrix relative to fragmented mixed fluid-solid flow velocities (Kern,  
 310 1995; Saxton and Rawls, 2006). While the addition of evolving saturation would extend validity of the model, it  
 311 would require implementation of pretransfer-functions for evolving material properties, which is beyond the  
 312 scope of this work. An important note on the points made above is the manner in which fluids are re-partitioned  
 313 after fragmentation. All fluids in fragmented solids are released, but this does not equate to free movement of the  
 314 fluids or a disconnection from the solids that confined them. Instead, the equations continue to connect the solids  
 315 and fluids through drag, viscous and virtual mass forces. Finally, the density of the fragmented solids is assumed  
 316 to be the initially set solid density. Any strain-induced density changes are assumed small relative to the initial  
 317 solid density ( $\frac{\rho_c}{\rho_s} \ll 1$ ).

#### 318 **Fluid Stresses**

319 The fluid stress tensor is determined by the pressure and the viscous terms (Equations 29 and 30).  
 320 Confined solids are assumed to be saturated and constant during the flow.

$$321 \quad 29. \mathbf{T}_u = P_f \mathbf{I} + \boldsymbol{\tau}_f$$

$$322 \quad 30. \boldsymbol{\tau}_f = \eta_f [\nabla \mathbf{u}_u + (\nabla \mathbf{u}_c)^t] - \frac{\eta_f}{\alpha_u} \mathcal{A}(\alpha_u) (\nabla \alpha_c (\mathbf{u}_u - \mathbf{u}_c) + (\mathbf{u}_c - \mathbf{u}_u) \nabla \alpha_c)$$

323 Where  $\mathbf{I}$  is the identity tensor,  $\boldsymbol{\tau}_f$  is the viscous stress tensor for fluids,  $P_f$  is the fluid pressure,  $\eta_f$  is the  
 324 dynamic viscosity of the fluids and  $\mathcal{A}$  is the mobility of the fluids at the interface with the solids that acts as a  
 325 phenomenological parameter (Pudasaini, 2012).

326 The fluid pressure acts only on the free fluids here, as the confined fluids are moved together with the  
 327 solids. In equation 30, the second term is related to the non-Newtonian viscous force induced by gradients in  
 328 solid concentration. The effect as described by Pudasaini (2012) is induced by a solid-concentration gradient. In  
 329 case of unconfined fluids and unstructured solids ( $f_{sf} = 1, f_{sf} = 1$ ). Within our flow description, we see no  
 330 direct reason to eliminate or alter this force with a variation in the fraction of confined fluids or structured solids.  
 331 We do only consider the interface between solids and free fluids as an agent that induces this effect, and  
 332 therefore the gradient of the gradient of the solids and confined fluids ( $\nabla(\alpha_s + f_{fc}\alpha_f) = \nabla\alpha_c$ ) is used instead of  
 333 the total solid phase ( $\nabla\alpha_s$ ).

### 334 Drag force and Virtual Mass

335 Our description of the drag force follows the work of Pudasaini (2012) and Pudasaini (2018), where a  
 336 generalized two-phase drag model is introduced and enhanced. We split their work into a contribution from the  
 337 fraction of structured solids ( $f_{sc}$ ) and unconfined fluids ( $1 - f_{fc}$ ) (Equation 31).

$$338 \quad 31. \quad C_{DG} = \frac{f_{sc}\alpha_c\alpha_u(\rho_c - \rho_f)g}{U_{T,c}(G(Re)) + S_p} (\mathbf{u}_u - \mathbf{u}_c)|\mathbf{u}_u - \mathbf{u}_c|^{j-1} + \frac{(1-f_{sc})\alpha_c\alpha_u(\rho_s - \rho_f)g}{U_{T,uc}(\mathcal{P}\mathcal{F}(Re_p) + (1-\mathcal{P})G(Re)) + S_p} (\mathbf{u}_u - \mathbf{u}_c)|\mathbf{u}_u - \mathbf{u}_c|^{j-1}$$

339 Where  $U_{T,c}$  is the terminal or settling velocity of the structures solids,  $U_{T,uc}$  is the terminal velocity of  
 340 the unconfined solids,  $\mathcal{P}$  is a factor that combines solid- and fluid like contributions to the drag force,  $G$  is the  
 341 solid-like drag contribution,  $\mathcal{F}$  is the fluid-like drag contribution and  $S_p$  is the smoothing function (Equation 32  
 342 and 34). The exponent  $j$  indicates the type of drag: linear ( $j = 0$ ) or quadratic ( $j = 1$ ).

343 Within the drag, the following functions are defined:

$$344 \quad 32. \quad F = \frac{\gamma}{180} \left(\frac{\alpha_f}{\alpha_s}\right)^3 Re_p, \quad G = \alpha_f^{M(Re_p)-1}$$

$$345 \quad 33. \quad S_p = \left(\frac{\mathcal{P}}{\alpha_c} + \frac{1-\mathcal{P}}{\alpha_u}\right)\mathcal{K}$$

$$346 \quad 34. \quad \mathcal{K} = |\alpha_c\mathbf{u}_c + \alpha_u\mathbf{u}_u| \approx 10 \text{ m s}^{-1}$$

347 Where  $M$  is a parameter that varies between 2.4 and 4.65 based on the Reynolds number (Pitman & Le,  
 348 2005). The factor  $\mathcal{P}$  that combines solid- and fluid like contributions to the drag, is dependent on the volumetric  
 349 solid content in the unconfined and unstructured materials ( $\mathcal{P} = \left(\frac{\alpha_s(1-f_{sc})}{\alpha_f(1-f_{fc})}\right)^m$  with  $m \approx 1$ ). Additionally we  
 350 assume the factor  $\mathcal{P}$ , is zero for drag originating from the structured solids. As stated by Pudasaini & Mergili  
 351 (2019) "As limiting cases:  $\mathcal{P}$  suitably models solid particles moving through a fluid". In our model, the drag  
 352 force acts on the unconfined fluid momentum ( $u_{uc}\alpha_f(1 - f_{fc})$ ). For interactions between unconfined fluids and  
 353 structured solids, larger blocks of solid structures are moving through fluids that contains solids of smaller size.

354 Virtual mass is similarly implemented based on the work of Pudasaini (2012) and Pudasaini & Mergili  
 355 (2019) (Equation 35). The adapted implementation considers the solids together with confined fluids to move  
 356 through a free fluid phase.

$$357 \quad 35. \quad C_{VMG} = \alpha_c\rho_u \left(\frac{1}{2} \left(\frac{1+2\alpha_c}{\alpha_u}\right)\right) \left(\left(\frac{\partial u_u}{\partial t} + \mathbf{u}_u \cdot \nabla \mathbf{u}_u\right) - \left(\frac{\partial u_c}{\partial t} + \mathbf{u}_c \cdot \nabla \mathbf{u}_c\right)\right)$$

358 Where  $C_{DG} = \frac{1}{2} \left(\frac{1+2\alpha_c}{\alpha_u}\right)$  is the drag coefficient.

### 359 **Boundary conditions**

360 Finally, following the work of Iverson & Denlinger (2001), Pitman & Le (2005) and Pudasaini (2012), a  
 361 boundary condition is applied to the surface elements that contact the flow (Equation 36).

$$362 \quad 36. \quad |\mathbf{S}| = N \tan(\phi)$$

363 Where  $N$  is the normal pressure on the surface element and  $\mathbf{S}$  is the shear stress.

### 364 **4-3 2.3 Depth-Averaging**

365 The majority of the depth-averaging in this work is analogous to the work of Pitman & Le (2005),  
 366 Pudasaini (2012) and Pudasaini & Mergili (2019). Depth-averaging through integration over the vertical extent of

Formatted: Normal, No bullets or numbering

Formatted: Font: (Default) Times New Roman, 10 pt, Bold

367 the flow can be done based on several useful and often-used assumptions:  $\frac{1}{h} \int_0^h x dh = \bar{x}$ , for the velocities ( $u_u$   
368 and  $u_c$ ), solid, fluid and confined fractions ( $\alpha_f$ ,  $\alpha_s$ ,  $f_{fc}$  and  $f_{sc}$ ) and material properties ( $\rho_u$ ,  $\phi$  and  $c$ ). Besides  
369 these similarities and an identical derivation of depth-averaged continuity equations, three major differences  
370 arise.

#### 371 i) Fluid pressure

372 Previous implementations of generalized two-phase debris flow equations have commonly assumed hydrostatic  
373 pressure ( $\frac{\partial p}{\partial z} = g^z$ ) (Pitman & Le, 2005; Pudasaini, 2012; Abe & Konagai, 2016). Here we follow this  
374 assumption for the fluid pressure at the base and solid pressure for unstructured material (Equations 37 and 38 ).

$$375 \quad 37. \quad P_{b_s, u} = -(1 - \gamma)\alpha_s g^z h$$

$$376 \quad 38. \quad P_{b_u} = -g^z h$$

377 Where  $\gamma = \frac{\rho_f}{\rho_s}$  is the density ratio (not to be confused with a tensor index when used in superscript) (-).

378 However, larger blocks of structure material can have contact with the basal topography. Due to density  
379 differences, larger blocks of solid structures are likely to move along the base (Pailhia & Pouliquen, 2009;  
380 George & Iverson, 2014). If these blocks are saturated, water pressure propagates through the solid matrix and  
381 hydrostatic pressure is retained. However, in cases of an unsaturated solid matrix that connects to the base,  
382 hydrostatic pressure is not present there. We introduce a basal fluid pressure propagation factor  $\mathcal{B}(\theta_{eff}, \bar{d}_{sc}, \dots)$   
383 which describes the fraction of fluid pressure propagated through a solid matrix (with  $\theta_{eff}$  the effective  
384 saturation,  $\bar{d}_{sc}$  the average size of structured solid matrix blocks). This results in a basal pressure equal to  
385 equation 39.

$$386 \quad 39. \quad P_{b_c} = -(1 - f_{sc})(1 - \gamma) \frac{(1 - f_{sc})\alpha_s}{(1 - f_{fc})\alpha_f} g^z h - f_{sc}(1 - \gamma) \mathcal{B} \frac{(f_{sc})\alpha_s}{(f_{fc})\alpha_f} g^z h$$

387 The basal pressure propagation factor ( $\mathcal{B}$ ) should theoretically depend, similarly to the pedotransfer  
388 function, mostly on saturation level, as a full saturation means perfect propagation of pressure through the  
389 mixture, and low saturation equates to minimal pressure propagation (Saxton and Rawls., 2006). Additionally it  
390 should depend on pedotransfer functions, and the size distribution of structured solid matrices within the  
391 mixture. For low-saturation levels, it can be assumed no fluid pressure is retained. Combined with an assumed  
392 soil matrix height identical to the total mixture height, this results in  $\mathcal{B} = 0$ . Assuming saturation of structures  
393 solids results in a full propagation of pressures and  $\mathcal{B} = 1$ .

#### 394 ii) Stress-Strain relationship

395 Depth-averaging the stress-strain relationship in equations 22 and 23 requires a vertical solution for the  
396 internal stress. First, we assume any non-normal vertical terms are zero (Equation 40). Commonly, Rankines  
397 earth pressure coefficients are used to express the lateral earth pressure by assuming vertical stress to be induced  
398 by the basal solid pressure (Equation 41 and 42) (Pitman & Le, 2005; Pudasaini, 2012; Abe & Konagai, 2016).

$$399 \quad 40. \quad \sigma^{zx} = \sigma^{zy} = \sigma^{yz} = \sigma^{xz} = 0$$

$$400 \quad 41. \quad \bar{\sigma}^{zz} = \frac{1}{2} P_{b_s}, \sigma^{zz}|_b = P_{b_s}$$

$$401 \quad 42. \quad K_a = \frac{1 - \sin(\phi)}{1 + \sin(\phi)}, \quad K_p = \frac{1 + \sin(\phi)}{1 - \sin(\phi)}$$

402 Here we enhance this with Bell's extension for cohesive soils (Equation 45) (Richard et al., 2017). This  
403 lateral normal-directed stress term is added to the full stress-strain solution.

$$404 \quad 43. \quad \bar{\sigma}_{xx} = K \sigma_{zz}|_b - 2c\sqrt{K} + \frac{1}{h} \int_0^h \sigma_{xx} dh$$

405 Finally, the gradient in pressure of the lateral interfaces between the mixture is added as a depth-  
406 averaged acceleration term (Equation 44).

$$407 \quad 44. \quad S_{x_c} = \alpha_c \left( \frac{1}{h} \left( \frac{\partial(h\sigma^{xx})}{\partial x} + \frac{\partial(h\sigma^{yx})}{\partial y} \right) \right) + \dots$$

#### 408 iii) Depth-averaging other terms

409 While the majority of terms allow for depth-averaging as proposed by Pudasaini (2012), an exception  
410 arises. Depth-averaging of the vertical viscosity terms is required. The non-Newtonian viscous terms for the fluid  
411 phase were derived assuming a vertical profile in the volumetric solid phase content. Here, we alter the

412 derivation to use this assumption only for the non-structured solids, as opposed to the structured solids where  
413  $\frac{\partial \alpha_s}{\partial z} = 0$ .

$$414 \quad 45. \int_b^s \frac{\partial}{\partial z} \left( \frac{\partial \alpha_s}{\partial z} (u_u - u_c) \right) dz = \left[ \frac{\partial \alpha_s}{\partial z} (u_u - u_c) \right]_b^s = (\bar{u}_u - \bar{u}_c) \left[ \frac{\partial \alpha_s}{\partial z} \right]_b^s = (\bar{u}_u - \bar{u}_c) \left[ \frac{\partial \alpha_s}{\partial z} \right]_b^s =$$

$$415 \quad \frac{(\bar{u}_u - \bar{u}_c)(1-f_{sc})\zeta \alpha_s}{h}$$

416 Where  $\zeta$  is the shape factor for the vertical distribution of solids (Pudasaini, 2012). Additionally, the  
417 momentum balance of Pudasaini (2012) ignores any deviatoric stress ( $\tau_{xy} = 0$ ), following Savage and Hutter  
418 (2007), and Pudasaini and Hutter (2007). Earlier this term was included by Iverson and Denlinger (2001), Pitman  
419 and Le (2005) and Abe & Kanogai (2016). Here we include these terms since a full stress-strain relationship is  
420 included.

#### 421 Basal frictions

422 Additionally we add the Darcy-Weisbach friction, which is a Chezy-type friction law for the fluid phase  
423 that provides drag (Delestre et al., 2014). This ensures that, without solid phase, a clear fluid does lose  
424 momentum due to friction from basal shear. This was successfully done in Bout et al. (2018) and was similarly  
425 assumed in Pudasaini and Fischer (2016) for fluid basal shear stress.

$$426 \quad 46. S_f = \frac{g}{n^2} \frac{u_u |u_u|}{h^{\frac{4}{3}}}$$

427 Where  $n$  is Manning's surface roughness coefficient.

#### 428 Depth-averaged equations

429 The following set of equations is thus finally achieved for depth-averaged flow over sloping terrain (Equations  
430 47-71).

$$431 \quad 47. \frac{\partial h}{\partial t} + \frac{\partial}{\partial x} [h(\alpha_u u_u + \alpha_c u_c)] + \frac{\partial}{\partial y} [h(\alpha_u u_u + \alpha_c u_c)] = R - I$$

$$432 \quad 48. \frac{\partial \alpha_c h}{\partial t} + \frac{\partial \alpha_c h u_c}{\partial x} + \frac{\partial \alpha_c h v_c}{\partial y} = 0$$

$$433 \quad 49. \frac{\partial \alpha_u h}{\partial t} + \frac{\partial \alpha_u h u_u}{\partial x} + \frac{\partial \alpha_u h v_u}{\partial y} = R - I$$

$$434 \quad 50. \frac{\partial}{\partial t} [\alpha_c h (u_c - \gamma_c C_{VM} (u_u - u_c))] + \frac{\partial}{\partial x} [\alpha_c h (u_c^2 - \gamma_c C_{VM} (u_u^2 - u_c^2))] + \frac{\partial}{\partial y} [\alpha_c h (u_c v_c -$$

$$435 \quad \gamma_c C_{VM} (u_u v_u - u_c v_c))] = h S_{x_c}$$

$$436 \quad 51. \frac{\partial}{\partial t} [\alpha_c h (v_c - \gamma_c C_{VM} (v_u - v_c))] + \frac{\partial}{\partial x} [\alpha_c h (u_s v_s - \gamma_c C_{VM} (u_u v_u - u_c v_c))] + \frac{\partial}{\partial y} [\alpha_c h (v_c^2 -$$

$$437 \quad \gamma_c C_{VM} (v_u^2 - v_c^2))] = h S_{y_c}$$

$$438 \quad 52. \frac{\partial}{\partial t} [\alpha_u h (u_u - \frac{\alpha_c}{\alpha_u} C_{VM} (u_u - u_c))] + \frac{\partial}{\partial x} [\alpha_u h (u_u^2 - \frac{\alpha_c}{\alpha_u} C_{VM} (u_u^2 - u_c^2) + \frac{\beta_{xu} h}{2})] + \frac{\partial}{\partial y} [\alpha_u h (u_u v_u -$$

$$439 \quad \gamma_c C_{VM} (u_u v_u - u_c v_c))] = h S_{x_u} - I u_u$$

$$440 \quad 53. \frac{\partial}{\partial t} [\alpha_u h (v_u - \frac{\alpha_c}{\alpha_u} C_{VM} (v_u - v_c))] + \frac{\partial}{\partial x} [\alpha_u h (u_u v_u - \frac{\alpha_c}{\alpha_u} C_{VM} (u_u v_u - u_c v_c))] + \frac{\partial}{\partial y} [\alpha_u h (v_u^2 -$$

$$441 \quad \gamma_c C_{VM} (v_u^2 - v_c^2) + \frac{\beta_{yu} h}{2})] = h S_{y_u} - I v_u$$

$$442$$

$$443 \quad 54. S_{x_c} = \alpha_c \left[ g^x + \frac{1}{h} \left( \frac{\partial(h\sigma^{xx})}{\partial x} + \frac{\partial(h\sigma^{yy})}{\partial y} \right) - P_{bc} \left( \frac{u_c}{|u_c|} \tan \phi + \epsilon \frac{\partial b}{\partial x} \right) - \epsilon \alpha_c \gamma_c p_{bu} \left[ \frac{\partial h}{\partial x} + \frac{\partial b}{\partial x} \right] + \right.$$

$$444 \quad \left. C_{DG} (u_u - u_c) |u_u - u_c|^{J-1} \right]$$

$$445 \quad 55. S_{y_c} = \alpha_c \left[ g^y + \frac{1}{h} \left( \frac{\partial(h\sigma^{xy})}{\partial x} + \frac{\partial(h\sigma^{yy})}{\partial y} \right) - P_{bc} \left( \frac{v_c}{|v_c|} \tan \phi + \epsilon \frac{\partial b}{\partial y} \right) - \epsilon \alpha_c \gamma_c p_{bu} \left[ \frac{\partial h}{\partial y} + \frac{\partial b}{\partial y} \right] + \right.$$

$$446 \quad \left. C_{DG} (v_u - v_c) |v_u - v_c|^{J-1} \right]$$

$$447$$

$$448 \quad 56. S_{x_u} = \alpha_u \left[ g^x - \frac{1}{2} \frac{p_{bu} h}{\alpha_u} \frac{\partial \alpha_c}{\partial x} + P_{bu} \frac{\partial b}{\partial x} - \frac{\mathcal{A} \eta_u}{\alpha_u} \left( 2 \frac{\partial^2 u_u}{\partial x^2} + \frac{\partial^2 v_u}{\partial xy} + \frac{\partial^2 u_u}{\partial y^2} - \frac{X u_u}{\epsilon^2 h^2} \right) + \frac{\mathcal{A} \eta_u}{\alpha_u} \left( 2 \frac{\partial}{\partial x} \left( \frac{\partial}{\partial x} (u_u - u_c) \right) + \right.$$

$$449 \quad \left. \frac{\partial}{\partial y} \left( \frac{\partial \alpha_c}{\partial x} (v_u - v_c) + \frac{\partial \alpha_u}{\partial y} (u_u - u_c) \right) \right) - \frac{\mathcal{A} \eta_u \zeta \alpha_s (1-f_{sc}) (u_u - u_c)}{\alpha_u h^2} - \frac{g}{n^2} \frac{u_u |u_u|}{h^{\frac{4}{3}}} \right] - \frac{1}{\gamma_c} C_{DG} (u_u -$$

$$450 \quad u_c) |u_u - u_c|^{J-1}$$

451 57.  $S_{y_u} = \alpha_u \left[ g^y - \frac{1}{2} \frac{P_{b_u} h}{\alpha_f} \frac{\partial \alpha_c}{\partial y} + P_{b_u} \frac{\partial b}{\partial y} - \frac{A \eta_u}{\alpha_u} \left( 2 \frac{\partial^2 u_f}{\partial y^2} + \frac{\partial^2 v_f}{\partial x y} + \frac{\partial^2 u_f}{\partial x^2} - \frac{X u_f}{\varepsilon^2 h^2} \right) + \frac{A \eta_u}{\alpha_c} \left( 2 \frac{\partial}{\partial y} \left( \frac{\partial}{\partial y} (v_u - \right. \right. \right.$

452  $v_c) + \frac{\partial}{\partial x} \left( \frac{\partial \alpha_c}{\partial y} (u_u - u_c) + \frac{\partial \alpha_c}{\partial x} (v_u - v_c) \right) \right) - \frac{A \eta_u \zeta \alpha_s (1 - f_{sc}) (v_u - v_c)}{\alpha_u h^2} - \frac{g}{n^2} \frac{v_u |u_u|}{h^{\frac{4}{3}}} \left. \right] - \frac{1}{\gamma_c} C_{DG} (v_u -$

453  $v_c) |\bar{u}_u - \bar{u}_c|^{J-1}$

454

455 58.  $P_{b_c} = -(1 - f_{sc})(1 - \gamma) \frac{(1 - f_{sc}) \alpha_s}{(1 - f_{fc}) \alpha_f} g^z h - f_{sc}(1 - \gamma) \frac{(f_{sc}) \alpha_s}{(f_{fc}) \alpha_f} g^z h$

456 59.  $P_{b_u} = -g^z h$

457 60.  $\gamma_c = \frac{\rho_u}{\rho_c}, \gamma = \frac{\rho_f}{\rho_s}$

458 61.  $C_{DG} = \frac{f_{sc} \alpha_c \alpha_u (\rho_c - \rho_f) g}{U_{T,c} (G(Re) + S_p)} + \frac{(1 - f_{sc}) \alpha_c \alpha_u (\rho_s - \rho_f) g}{U_{T,uc} (PF(Re_p) + (1 - P)G(Re) + S_p)}$

459 62.  $S_p = \left( \frac{p}{\alpha_c} + \frac{1 - p}{\alpha_u} \right) \mathcal{K}$

460 63.  $\mathcal{K} = |\alpha_c \mathbf{u}_c + \alpha_u \mathbf{u}_u|$

461 64.  $F = \frac{\gamma}{180} \left( \frac{\alpha_f}{\alpha_s} \right)^3 Re_p, G = \alpha_f^{M(Re_p)-1}, Re_p = \frac{\rho_f d U_c}{\eta_f}, N_R = \frac{\sqrt{gLH} \rho_f}{\alpha_f \eta_f}, N_{RA} = \frac{\sqrt{gLH} \rho_f}{A \eta_f}$

462 65.  $C_{vm} = \left( \frac{1}{2} \left( \frac{1 + 2\alpha_c}{\alpha_u} \right) \right)$

463 66.  $\hat{\sigma} = \sigma^{\alpha\gamma} \hat{\omega}^{\beta\gamma} + \sigma^{\gamma\beta} \hat{\omega}^{\alpha\gamma} + 2G \hat{e}^{\alpha\beta} + K \hat{e}^{\gamma\gamma} \delta^{\alpha\beta} - \lambda \left[ 9K \sin \psi \delta^{\alpha\beta} + \frac{G}{\sqrt{J_2}} S^{\alpha\beta} \right]$

464 67.  $\lambda = \frac{3\alpha K \hat{e}^{\gamma\gamma} + \left( \frac{G}{\sqrt{J_2}} \right) S^{\alpha\beta} \hat{e}^{\alpha\beta}}{27\alpha_\phi K \sin \psi + G}$

465 68.  $K = \frac{E}{3(1-2\nu)}, G = \frac{E}{2(1+\nu)}$

466 69.  $\sigma^{\alpha\beta} = S^{\alpha\beta} + \frac{1}{3} \sigma^{\gamma\gamma} \delta^{\alpha\beta}$

467 70.  $\hat{e}^{\alpha\beta} = \frac{1}{2} \left( \frac{\partial v^\alpha}{\partial x^\beta} - \frac{\partial v^\beta}{\partial x^\alpha} \right), \hat{\omega}^{\alpha\beta} = \frac{1}{2} \left( \frac{\partial v^\alpha}{\partial x^\beta} + \frac{\partial v^\beta}{\partial x^\alpha} \right)$

468 71.  $\alpha_\phi = \frac{\tan(\phi)}{\sqrt{9+12 \tan^2 \phi}}, k_c = \frac{3c}{\sqrt{9+12 \tan^2 \phi}}$

471 Where X is the shape factor for vertical shearing of the fluid ( $X \approx 3$  in Iverson & Denlinger, 2001), R is the  
472 precipitation rate and I is the infiltration rate.

473  
474 **Closing the equations**

475 Viscosity is estimated using the empirical expression from O'Brien and Julien (1985), which relates dynamic  
476 viscosity to the solid concentration of the fluid (Equation 72).

477 72.  $\eta = \alpha e^{\beta \alpha_s}$

478 Where  $\alpha$  is the first viscosity parameter and  $\beta$  the second viscosity parameter.

479 Finally, the settling velocity of small ( $d < 100 \mu m$ ) grains is estimated by Stokes equations for a  
480 homogeneous sphere in water. For larger grains ( $> 1 mm$ ), the equation by Zanke (1977) is used (Equation 30).

481 73.  $U_T = 10 \frac{\eta^2}{\rho_f d} \left( \sqrt{1 + \frac{0.01 \left( \frac{\rho_s - \rho_f}{\rho_f} \right) g d^3}{\eta}} - 1 \right)$

482 In which  $U_T$  is the settling (or terminal) velocity of a solid grain,  $\eta$  is the dynamic viscosity of the fluid,  
483  $\rho_f$  is the density of the fluid,  $\rho_s$  is the density of the solids, d is the grain diameter (m)

484  
485 **21.4 Implementation in the Material Point Method numerical scheme**

486 Implementing the presented set of equations into a numerical scheme requires considerations of that  
487 schemes limitations and strengths (Stomakhin et al., 2013). Fluid dynamics are almost exclusively solved using

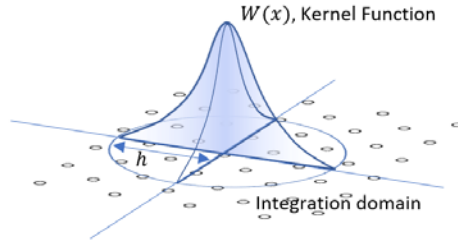
488 an Eulerian finite element solution (Delestre et al., 2014; Bout et al., 2018). The diffusive advection part of such  
 489 scheme typically doesn't degrade the quality of modelling results. Solid material however is commonly  
 490 simulated with higher accuracy using an Lagrangian finite element method or discrete element method (Maurel  
 491 & Cumbescure, 2008; Stomakhin et al., 2013). Such schemes more easily allow for the material to maintain its  
 492 physical properties during movement. Additionally, advection in these schemes does not artificially diffuse the  
 493 material since the material itself is discretized, instead of the space (grid) on which the equations are solved. In  
 494 our case, the material point method (MPM) provides an appropriate tool to implement the set of presented  
 495 equations (Bui et al., 2008; Maurel & Cumbescure, 2008; Stomakhin et al., 2013). Numerous existing modelling  
 496 studies have implemented in this method (Pastor et al., 2007; Pastor et al., 2008; Abe & Kanogai, 2016). Here,  
 497 we use the MPM method to create a two-phase scheme. This allows the usage of finite elements aspects for the  
 498 fluid dynamics, which are so successfully described by the that method (particularly for water in larger areas, see  
 499 Bout et al., 2018).

### 500 Mathematical Framework

501 The mathematic framework of smooth-particles solves differential equations using discretized volumes  
 502 of mass represented by kernel functions (Libersky & Petschek, 1991; Bui et al., 2008; Stomakhin et al., 2013).  
 503 Here, we use the cubic spline kernel as used by Monaghan (2000) (Equation 74).

$$504 \quad 74. \quad W(r, h) = \begin{cases} \frac{10}{7\pi h^2} \left(1 - \frac{3}{2}q^2 + \frac{3}{4}q^3\right) & 0 \leq |q| \leq 2 \\ \frac{10}{28\pi h^2} (2 - q)^3 & 1 \leq |q| < 2 \\ 0 & |q| \geq 2 \end{cases} \quad |q| \geq 2 \mid q < 0$$

505 Where  $r$  is the distance,  $h$  is the kernel size and  $q$  is the normalized distance ( $q = \frac{r}{h}$ )



506  
 507 *Figure 2 Example of a kernel function used as integration domain for mathematical operations.*

508 Using this function mathematical operators can be defined. The average is calculated using a weighted  
 509 sum of particle values (Equation 75) while the derivative depends on the function values and the derivative of  
 510 the kernel by means of the chain rule (Equation 76) (Libersky & Petschek, 1991; Bui et al., 2008).

$$511 \quad 75. \quad \langle f(x) \rangle = \sum_{j=1}^N \frac{m_j}{\rho_j} f(x_j) W(x - x_j, h)$$

$$512 \quad 76. \quad \left\langle \frac{\partial f(x)}{\partial x} \right\rangle = \sum_{j=1}^N \frac{m_j}{\rho_j} f(x_j) \frac{\partial W_{ij}}{\partial x_i}$$

513 Where  $W_{ij} = W(x_i - x_j, h)$  is the weight of particle  $j$  to particle  $i$ ,  $r = |x_i - x_j|$  is the distance  
 514 between two particles. The derivative of the weight function is defined by equation 77.

$$515 \quad 77. \quad \frac{\partial W_{ij}}{\partial x_i} = \frac{x_i - x_j}{r} \frac{\partial W_{ij}}{\partial r}$$

516 Using these tools, the momentum equations for the particles can be defined (Equations 78-84). Here, we  
 517 follow Monaghan (1999) and Bui et al. (2008) for the definition of artificial numerical forces related to stability.  
 518 Additionally, stress-based forces are calculated on the particle level, while other momentum source terms are  
 519 solved on a Eulerian grid with spacing  $h$  (identical to the kernel size).

$$520 \quad 78. \quad \frac{dv_i^\alpha}{dt} = \frac{1}{m_i} (F_g + F_{grid}) + \sum_{j=1}^N m_j \left( \frac{\sigma_j^{\alpha\beta}}{\rho_j^2} + \frac{\sigma_j^{\alpha\beta}}{\rho_j^2} + F_{ij}^n R_{ij}^{\alpha\beta} + \Pi_{ij} \delta^{\alpha\beta} \right) \frac{\partial W_{ij}}{\partial x_i^\beta}$$

$$521 \quad 79. \quad \dot{\epsilon}^{\alpha\beta} = \frac{1}{2} \left( \sum_{j=1}^N \frac{m_j}{\rho_j} (v_j^\alpha - v_i^\alpha) \frac{\partial W_{ij}}{\partial x_i^\beta} + \sum_{j=1}^N \frac{m_j}{\rho_j} (v_j^\beta - v_i^\beta) \frac{\partial W_{ij}}{\partial x_i^\alpha} \right)$$

$$\begin{aligned}
522 \quad 80. \quad \dot{\omega}^{\alpha\beta} &= \frac{1}{2} \left( \sum_{j=1}^N \frac{m_j}{\rho_j} (v_j^\alpha - v_i^\alpha) \frac{\partial W_{ij}}{\partial x_i^\beta} - \sum_{j=1}^N \frac{m_j}{\rho_j} (v_j^\beta - v_i^\beta) \frac{\partial W_{ij}}{\partial x_i^\alpha} \right) \\
523 \quad 81. \quad \frac{d\sigma_{\alpha\beta}}{dt} &= \sigma_i^{\alpha\gamma} \dot{\omega}_i^{\beta\gamma} + \sigma_i^{\gamma\beta} \dot{\omega}_i^{\alpha\gamma} + 2G_i \dot{\epsilon}_i^{\alpha\beta} + K_i \epsilon^{\gamma\gamma} \delta_i^{\alpha\beta} - \dot{\lambda}_i \left[ 9K_i \sin\psi_i \delta^{\alpha\beta} + \frac{G_i}{\sqrt{J_{2i}}} S_i^{\alpha\beta} \right] \\
524 \quad 82. \quad \dot{\lambda}_i &= \frac{3\alpha K_i \epsilon_i^{\gamma\gamma} + \left( \frac{G_i}{\sqrt{J_{2i}}} \right) S_i^{\alpha\beta} \dot{\epsilon}_i^{\alpha\beta}}{27\alpha_\phi K_i \sin\psi_i + G_i}
\end{aligned}$$

525 Where  $i, j$  are indices indicating the particle,  $\Pi_{ij}$  is an artificial viscous force as defined by equations 83  
526 and 84 and  $F_{ij}^n R_{ij}^{\alpha\beta}$  is an artificial stress term as defined by equations 85 and 86.

$$\begin{aligned}
527 \quad 83. \quad \Pi_{ij} &= \begin{cases} \frac{\alpha_\Pi u_{sound} \rho_{ij} \phi_{ij} + \beta_\Pi \phi^2}{\rho_{ij}} v_{ij} \cdot x_{ij} < 0 \\ 0 & v_{ij} \cdot x_{ij} \geq 0 \end{cases} \\
528 \quad 84. \quad \phi_{ij} &= \frac{h_{ij} v_{ij} x_{ij}}{|x_{ij}|^2 + 0.01 h_{ij}^2}, \quad x_{ij} = x_i - x_j, \quad v_{ij} = v_i - v_j, \quad h_{ij} = \frac{1}{2}(h_i + h_j) \\
529 \quad 85. \quad F_{ij}^n R_{ij}^{\alpha\beta} &= \left[ \frac{W_{ij}}{W(d_0, h)} \right]^n (R_i^{\alpha\beta} + R_j^{\alpha\beta}) \\
530 \quad 86. \quad \overline{R}_i^{\gamma\gamma} &= -\frac{\epsilon_0 \sigma_i^{\gamma\gamma}}{\rho_i^2}
\end{aligned}$$

531 Where  $\epsilon_0$  is a small parameter ranging from 0 to 1,  $\alpha_\Pi$  and  $\beta_\Pi$  are constants in the artificial viscous  
532 force (often chosen close to 1),  $u_{sound}$  is the speed of sound in the material.

533 The conversion from particles to gridded values and reversed depends on a grid basis function that  
534 weighs the influence of particle values for a grid center. Here, a function derived from dyadic products of one-  
535 dimensional cubic B-splines is used as was done by Steffen et al. (2008) and Stomakhin et al. (2013) (Equation  
536 84).

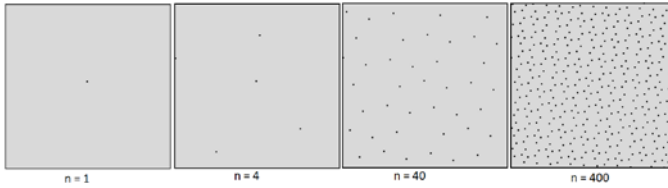
$$537 \quad 87. \quad N(x) = N(x^x) * N(x^y), \quad N(x) = \begin{cases} \frac{1}{2}|x|^3 - x^2 + \frac{2}{3} & 0 \leq |x| \leq 2 \\ -\frac{1}{6}|x|^3 + x^2 - 2|x| + \frac{4}{3} & 1 \leq |x| < 2 \\ 0 & |x| \geq 2 \mid x = 0 \end{cases}$$

### 538 Particle placement

539 Particle placement is typically done in a constant pattern, as initial conditions have some constant  
540 density. The simplest approach is a regular square or triangular network, with particles on the corners of the  
541 network. Here, we use an approach that is more adaptable to spatially-varying initial flow height. The  $R_2$   
542 sequence approaches, with a regular quasirandom sequence, a set of evenly distributed points within a square  
543 (Roberts, 2020) (Equation 85).

$$544 \quad 88. \quad x_n = n\alpha \bmod 1, \quad \alpha = \left( \frac{1}{c_p}, \frac{1}{c_p^2} \right)$$

545 Where  $x_n$  is the relative location of the  $n^{\text{th}}$  particle within a gridcell,  $c_p = \left( \frac{9+\sqrt{69}}{18} \right)^{\frac{1}{3}} + \left( \frac{9-\sqrt{69}}{18} \right)^{\frac{1}{3}} \approx$   
546 1.32471795572 is the plastic constant.

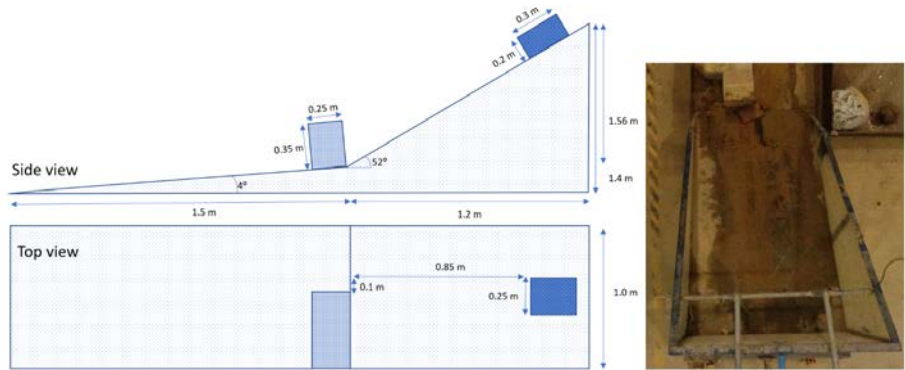


547  
548 *Figure 3 Example particle distributions using the  $R_2$  sequence, note that, while not all particles are*  
549 *equidistant, the method produces distributed particle patterns that adapt well to varying density.*

550 The number of particles placed for a particular flow height depends on the particle volume  $V_j$ , which is  
551 taken as a global constant during the simulation.

552 **2.3. Flume Experiments**  
 553 **2.3.1. Flume Setup**

554 In order to validate the presented model, several controlled experiments were performed and reproduced  
 555 using the developed equations. The flume setup consists of a steep incline, followed by a near-flat runout plane  
 556 (Figure 3). ~~A massive obstacle is placed on the separation point of the two planes. This~~ ~~On the separation point of~~  
 557 ~~the two planes, a massive and attached obstacle is present that~~ blocks the path of two fifths of the ~~width of the~~  
 558 moving material. For the exact dimensions of both the flume parts and the obstacle, see figure 3.



559 Figure 4 The dimensions of the flume experiment setup used in this work.  
 560

561 Two tests were performed whereby a cohesive granular matrix was released at the upper part of the  
 562 flume setup. Both of these volumes had dimensions of 0.2x0.3x0.25 meter (height,length,width). For both of  
 563 these materials, a mixture high-organic content silty-clay soils where used. The materials strength parameters  
 564 were obtained using tri-axial testing (Cohesion, internal friction angle Youngs modulus and Poisson Ration. The  
 565 first set of materials properties where  $c = 26.7$  kPa and  $\phi = 28^\circ$ . The second set materials properties where  $c =$   
 566  $18.3$  kPa and  $\phi = 27^\circ$ . For both of the events, pre-and post release elevations models were made using  
 567 photogrammetry. The model was set up to replicate the situations using the measured input parameters.  
 568 Numerical settings were chosen as  $\{\alpha_s = 0.5, \alpha_f = 0.5, f_{sc} = 1.0, f_{fc} = 1.0, \rho_f = 1000, \rho_s = 2400, E = 12 \cdot$   
 569  $10^6$  Pa,  $K = 23 \cdot 10^6$  Pa,  $\psi = 0, \alpha_{\Pi} = 1, \beta_{\Pi} = 1, X, \zeta, j = 2, u_{sound} = 600, dx = 10, V_i = , h = 10, n =$   
 570  $0.1, \alpha = 1, \beta = 10, M = 2.4, B = 0, N_R = 15000, N_{RA} = 30\}$ . Calibration was performed by means of input  
 571 variation. The solid fraction, and elastic and bulk modulus were varied between 20 and 200 percent of their  
 572 original values with increments of 10 percent. Accuracy was assessed based on the percentage accuracy of the  
 573 deposition (comparison of modelled vs observed presence of material).

574 **2.3.2. Results**

575 Both the mapped extent of the material after flume experiments, as the simulation results are shown in  
 576 figure 5. Calibrated values for the simulations are  $\{\alpha_s = 0.45, E = 21.6 \cdot 10^6$  Pa,  $K = 13.8 \cdot 10^6$  Pa $\}$ .

**Formatted:** Outline numbered + Level: 1 + Numbering  
 Style: 1, 2, 3, ... + Start at: 1 + Alignment: Left + Aligned  
 at: 0.63 cm + Indent at: 1.27 cm

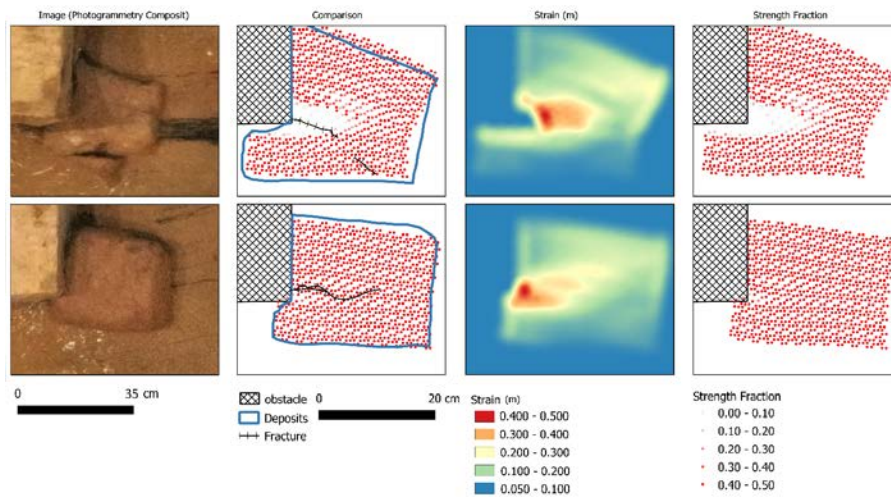
**Formatted:** Font: (Default) Times New Roman, 10 pt,  
 Bold

**Formatted:** Outline numbered + Level: 2 + Numbering  
 Style: 1, 2, 3, ... + Start at: 1 + Alignment: Left + Aligned  
 at: 0.63 cm + Indent at: 1.27 cm

**Formatted:** Font: (Default) Times New Roman, 10 pt,  
 Bold

**Formatted:** Outline numbered + Level: 2 + Numbering  
 Style: 1, 2, 3, ... + Start at: 1 + Alignment: Left + Aligned  
 at: 0.63 cm + Indent at: 1.27 cm





577  
 578 *Figure 5 A comparison of the final deposits of the simulations and the mapped final deposits and cracks*  
 579 *within the material. From left to right: Photogrammetry mosaic, comparison of simulation results to mapped*  
 580 *flume experiment, strain, final strength fraction remaining.*

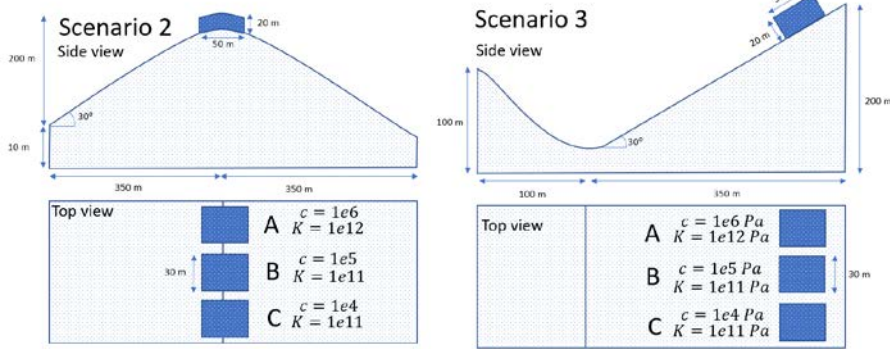
581 As soon as the block of material impacts the obstacle, stress increases as the moving objects is  
 582 deformed. This stress quickly propagates through the object. Within the scenario with lower cohesive strength,  
 583 as soon as the stress reached beyond the yield strength, degradation of strength parameters took place. In the  
 584 results, a fracture line developed along the corner of the obstacle into the length direction of the moving mass.  
 585 Eventually, this fracture developed to half the length of the moving body and severe deformation resulted. As  
 586 was observed from the tests, the first material experienced a critical fracture while the second test resulted in  
 587 moderate deformation near the impact location. Generally, the results compare well with the observed patters,  
 588 although the exact shape of the fracture is not replicated. Several reasons might be the cause of the moderately  
 589 accurate fracture patterns. Other studies used a more controlled setup where uncertainties in applied stress and  
 590 material properties were reduced. Furthermore, the homogeneity of the material used in the tests can not  
 591 completely assumed. Realistically, minor alterations in compression used to create the clay blocks has left spatial  
 592 variation in density, cohesion and other strength parameters.

### 593 4.3. Numerical Tests

#### 594 4.1 Numerical Setup

595 In order to further investigate some of the behaviors of the model, and highlight the novel types of mass  
 596 movement dynamics that the model implements, several numerical tests have been performed. The setup of these  
 597 tests is shown in figure 6.

598



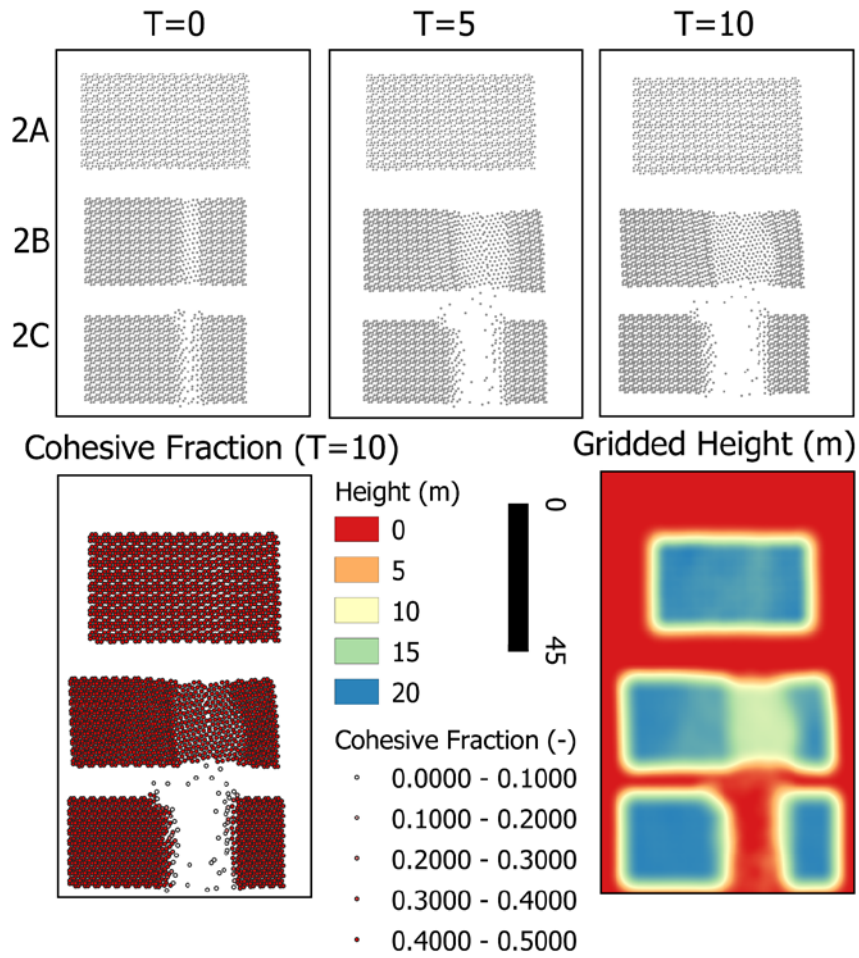
599  
600 Figure 6 The dimensions of the numerical experiment setups used in this work. Setup 1 (left) and Setup 2 (right)

601 Numerical settings were chosen for three different blocks with equal volume but distinct properties.  
602 Cohesive strength and the bulk modulus were varied (see figure 6). Remaining parameters were chosen as  
603  $\{\alpha_s = 0.5, \alpha_f = 0.5, f_{sc} = 1.0, f_{fc} = 1.0, \rho_f = 1000 \text{ kgm}^{-3}, \rho_s = 2400 \text{ kgm}^{-3}, E = 1e12 \text{ Pa}, \psi = 0, \alpha_{\Pi} =$   
604  $1, \beta_{\Pi} = 1, X, \zeta, j = 2, u_{sound} = 600 \text{ ms}^{-1}, dx = 10 \text{ m}, V_l, h = 10 \text{ m}, n = 0.1, \alpha = 1, \beta = 10, M = 2.4, \mathcal{B} =$   
605  $0, N_R = 15000, N_{RA} = 30\}$ .

606 **4.2.3.1 Results**

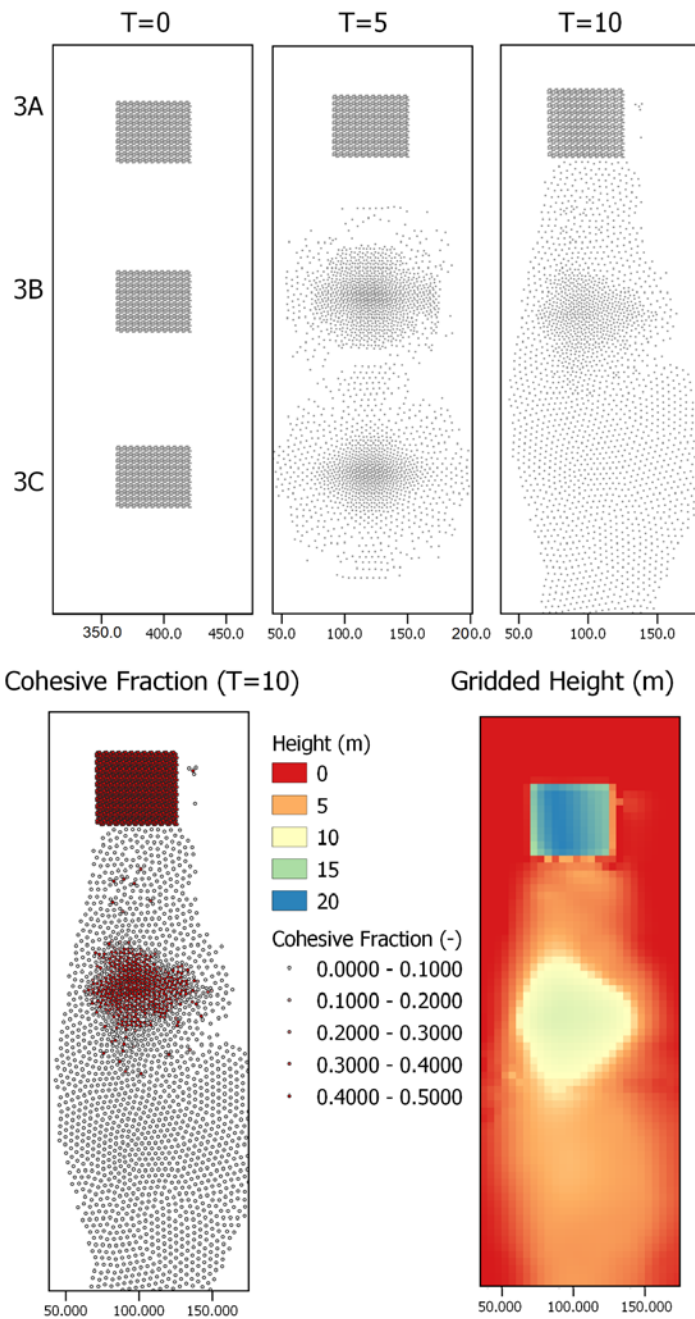
607 Several time-slices for the described numerical scenarios are shown in figure 7 and 8.

608



609

610 *Figure 7 Several time-slices for numerical scenarios 2(A/B/C). See figure 6 for the dimensions and*  
 611 *terrain setup.*



612  
613 *Figure 8 Several time-slices for numerical scenarios 3(A/B/C). See figure 6 for the dimensions and terrain setup.*

614 Fractures develop in the mass movements based on acceleration differences and cohesive strength. For  
615 scenario 2A, the stress state does not reach beyond the yield surface, and all material is moved as a single block.  
616 Scenario 2B, which features lowered cohesive strength, fractures and the masses separate based on the  
617 acceleration caused by slopes.

618 Fracturing behavior can occur in MPM schemes due to numerical limitations inherent in the usage of a  
619 limited integration domain. Here, validation of real physically-based fracturing is present in the remaining  
620 cohesive fraction. This value only reduces in case of plastic yield, where increasing strain degrades strength  
621 parameters according to our proposed criteria. Numerical fractures would thus have a cohesive fraction of 1. In  
622 all simulated scenarios, such numerical issues were not observed.

623 Fragmentation occurs due to spatial variation in acceleration in the case of scenario 3A and 3B. For  
624 scenario 3A, the yield surface is not reached and the original structure of the mass is maintained during  
625 movement. For 3C, fragmentation is induced by lateral pressure and buoyancy forces alone. Scenario 3B  
626 experiences slight fragmentation at the edges of the mass, but predominantly fragments when reaching the  
627 valley, after which part of the material is accelerated to count to the velocity of the mass. For all the shown  
628 simulations, fragmentation does not lead to significant phase separation since virtual mass and drag forces  
629 converge the separate phase velocities to their mixture-averaged velocity. The strength of these forces partly  
630 depends on the parameters, effects of more immediate phase-separation could be studied if other parameters are  
631 used as input.

#### 632 **5.4. Discussion**

633 A variety of existing landslide models simulate the behavior of lateral connected material through a  
634 non-linear, non-Newtonian viscous relationship (Boetticher et al., 2016; Fornes et al., 2017; Pudasaini &  
635 Mergili, 2019; Greco et al., 2019). These relationships include a yield stress and are usually regularized to  
636 prevent singularities from occurring. While this approach is incredibly powerful, it is fundamentally different  
637 from the work proposed here. These viscous approaches do not distinguish between elastic or plastic  
638 deformation, and typically ignore deformations if stress is insufficient. Additionally, fracturing is not  
639 implemented in these models. The approach taken in this work attempts to simulate a full stress-strain  
640 relationship with Mohr-Coulomb type yield surface. This does provide new types of behavior and can be  
641 combined with non-Newtonian viscous approaches as mentioned above. A major downside to the presented  
642 work is the steep increase in computational time required to maintain an accurate and stable simulation.  
643 Commonly, an increase of near a 100 times has been observed during the development of the presented model.

644 The presented model shows a good likeness to flume experiments and numerical tests highlight  
645 behavior that is commonly observed for landslide movements. There are however, inherent scaling issues and the  
646 material used in the flume experiments is unlikely to form larger landslide masses. The measured physical  
647 strength parameters of the material used in the flume experiments would not allow for sustained structured  
648 movement at larger scales. There is thus the need for more, real-scale, validation cases. The application of the  
649 presented type of model is most directly noticeable for block-type landslide movements that have fragmented  
650 either upon impact of some obstacle or during transition phase. Of importance here is that the moment of  
651 fragmentation is often not reported in studies on fast-moving landslides, potentially due to the complexities in  
652 knowing the details on this behavior from post-event evidence. Validation would therefore have to occur on  
653 cases where deposits are not fully fragmented, indicating that this process was ongoing during the whole  
654 movement duration. The spatial extent of initiation and deposition would then allow validation of the model.  
655 Another major opportunity for validation of the novel aspects of the model is the full three-dimensional  
656 application to landslides that were reported to have lubrication effects due to fragmentation of lower fraction of  
657 flow due to shear.

658 An important point of consideration in the development of complex multi-process generalized models is  
659 the applicability. As a detailed investigative research tool, these models provide a basic scenario of usage.  
660 However, both for research and beyond this, in applicability in disaster risk reduction decision support, the  
661 benefit drawn from these models depends on the practical requirement for parameterization and the  
662 computational demands for simulation. With an increasing complexity in the description of multi-process  
663 mechanics comes the requirement of more measured or estimated physical parameters. Inspection of the  
664 presented method shows that in principle, a minor amount of new parameters are introduced. The cohesive  
665 strength, a major focus of the model, becomes highly important depending on the type of movement being  
666 investigated. Additionally, the bulk and elastic modulus are required. These three parameters are common  
667 simulation parameters in geotechnical research and can be obtained from common tests on sampled material  
668 (Alsaman et al., 2015). Finally, the basal pressure propagation parameter ( $B$ ) is introduced. However, within  
669 this work, the value of this parameter is chosen to have a constant value of one. As a result, the model does  
670 require additional parameters, although these are relatively easy to obtain with accuracy.

671 There are a variety of aspects of the model that could be significantly improved. Here, we list several  
672 major opportunities of future research.

673 **1) Groundwater mechanics**

674 The presented model allows for the a solid or granular matrix to be present within the flow. We have  
675 assumed the flows in and out of these matrices are sufficiently small to be ignored. In reality, there is a  
676 fluid flux in and out of structured solids. This could occur both due to pressure differences as due to  
677 stress and strain of the structured solids. Implementing this kind of mechanics requires a dynamic,  
678 solid-properties dependent, soil water retention curve (Van Looy et al., 2017). An example of MPM soil  
679 mechanics with dynamic groundwater implementation can be found in Bandera et al. (2016).

680 **2) Implementing Entrainment and Deposition**

681 Current equations for entrainment (erosion with major grain-grain interactions) is limited to  
682 unstructured mixture flows (Iverson, 2012; Iverson & Ouyang, 2015; Cuomo et al., 2016; Pudasaini &  
683 Fischer, 2016). Extending these models to include a contribution from structured solids would be  
684 required to implement entrainment in the presented work.

685 **3) Separation of phases**

686 A major assumption in the presented work is that the velocities of structured solids, free solids and  
687 confined fluids are all equal. In reality, there might be separation of structured and free solids phases.  
688 Additionally, we already discussed the possibility of in-and outflux of confined fluids from the solid  
689 matrix. Recent innovations on three-phase mixture flows might be used to extend the presented work to  
690 a three, four or five-phase model by separating free solids, confined fluids or adding a Bingham-viscous  
691 solid-fluid phase (Pudasaini & Mergili, 2019). However, while this would implement an additional  
692 process, it would significantly increase complexity of the equations (in an exponential manner with  
693 relation to the number of phases) and the numerical solutions which could hinder practical applicability.

694 **4) Application to large, slow moving landslides.**

695 When confined fluids would act as a distinct phase, guided by the mechanics of water flow in granular  
696 matrix, ground water pressures and movement through the structured solids could be described. This  
697 might enable the model to do detailed deformation/groundwater simulation of large slow-moving  
698 landslides.

699 **5) Numerical Improvements**

700 Numerical techniques for particle-based discretized methods (SPH, MPM) have been proposed in the  
701 literature. A common issue is numerical fracturing of materials when particle strain increases beyond  
702 the length of the kernel function. Then, the connection between particles is lost and fracturing occurs as  
703 an artifact of the numerical method. This issue is partly solved by the artificial stress term as is also  
704 used by Bui et al. (2008). Additionally, geometric subdivide, as used by Xu et al. (2012) and Li et al.  
705 (2015), could counter these artificial fractures. Implementing this technique does require additional  
706 work to maintain mass and momentum conservation.

707 **6) Three-dimensional solutions**

708 In a variety of scenarios, the assumptions made in depth-averaged application of flow models are  
709 invalid. A common example is the impact of mass movements into lakes, or other large water bodies. In  
710 such cases, the vertical velocity and concentration variables are not well-described by their depth-  
711 averaged counterparts. Additionally, the lubrication effect of basal fragmentation of landslides due to  
712 shear can not be described without velocity-profiles and a vertical stress-solution. Full three-  
713 dimensional application would therefore have the potential to increase understanding on these important  
714 processes.

715 **5. Conclusions**

716 We have presented a novel generalized mass movement model that can describe both unstructured  
717 mixture flows and Structured movements of Mohr-Coulomb type material. The presented equations are part of  
718 the continuous development of the OpenLISEM Hazard model, an open-source tool for physically-based multi-  
719 hazard simulations. The model builds on the works of Pudasaini (2012) and Bui et al. (2008) to develop a single  
720 holistic set of equations. The model was implemented in a GPU-based Material Point Method (MPM) Code. The  
721 equations were validated on flume experiments and numerical tests, that highlight the new movement dynamics  
722 possible with the presented model. The integration of cohesive structure and a full stress-strain relationship for  
723 the structured solids allows for movement of block-type slides as a single whole. Interactions with terrain, other  
724 flow masses or obstacles lead to elastic-plastic deformation and eventually fragmentation. This type of self-  
725 alteration of flow properties is novel with mass movement models. Although the presented equations can provide  
726 additional detail for specific mass movement types, applicability of the model for real events need to be  
727 investigated as computational costs are significantly increased.

728 The presented simulation both validate the basic behavior of the model, as well as highlight the types of  
729 flow dynamics made possible by the presented equations. The models dependency of breaking to cohesive  
730 strength and internal friction angle matches the flume experiments. The numerical examples show commonly-  
731 described behavior for landslide movements. Although the simulations compare well to the flume experiments,  
732 validation is required for real-scale application to various types of mass movements. Additionally, the presented  
733 equations still lack descriptions of processes that might become important. Separating the fluid and solid phases  
734 such as done by Pudasaini & Mergili (2019), could improve flow dynamics and phase separation. With added  
735 ground-water mechanics, such as done in Bandera et al. (2016), slow-moving landslide simulations might be  
736 described.

#### 737 **6. Code and Data Availability**

738 All code and data used within this work are made open-source as part of the continuous development of  
739 the OpenLISEM Hazard model under the GNU General Public Licence v3.0. The code and the data are hosted  
740 on Github (<https://github.com/bastianvandenbout/OpenLISEM-Hazard-2.0-Pre-Release>). Both binaries  
741 and a copy of the source code are also available on Sourceforge, where the manual and compilation guide can  
742 similarly be found (<https://sourceforge.net/projects/lisem/>). Finally, more information can be found at the blog  
743 (<https://blog.utwente.nl/lisem/>)

744 The software, and its user interface, are written for windows, but platform independent libraries are  
745 used and compilation might be performed on other platforms.  
746 Hardware requirements for the usage of the model are a 64-bit Operating system that can compile all required  
747 external libraries (see the manual for a full list and description). A graphical processing unit conforming to at  
748 least the OpenCL 1.2 standard and support for both OpenGL 4.2 and OpenGL/OpenCL interoperability.  
749 Additionally, an approximate 500 mb of hard drive space and 750 mb of memory must be available.

750

751	<b>Appendix A. List of Symbols</b>
752	$h$ is the flow height
753	$s$ is the solid phase
754	$f$ is the fluid phase
755	$sc$ is the structured solid phase
756	$fc$ is the confined fluid phase
757	$\rho_f$ is the density of fluids
758	$\rho_s$ is the density of solids
759	$\alpha_f$ is the volumetric fluid phase fraction
760	$\alpha_s$ is the volumetric solid phase fraction
761	$f_{sc}$ is the fraction of solids that is structured (confining)
762	$f_{fc}$ is the fraction of fluids that is confined
763	$\alpha_c$ is the volumetric fraction of solids, structured solids and confined fluids
764	$\alpha_u$ is the volumetric fraction of free fluids (unconfined phase).
765	$\rho_{sc}$ is the volume-averaged density of the solids and confined fluids
766	$\mathbf{u}_u$ is the velocity of the unconfined phase (free fluids)
767	$\mathbf{u}_c$ is the velocity of the solids, confining solids and confined fluids
768	$\mathbf{u}_s$ is the velocity of the solids
769	$\mathbf{f}$ is the body force
770	$\mathbf{M}_{DG}$ is the drag force
771	$\mathbf{M}_{vm}$ is the virtual mass force
772	$\mathbf{T}_c$ is the stress tensor for eh solids, confining solids and confined fluids
773	$\mathbf{T}_u$ is the stress tensor for the free fluid phase
774	$\boldsymbol{\sigma}$ is the stress tensor
775	$\dot{\boldsymbol{s}}$ is the deviatoric shear stress rate tensor
776	$\delta$ is the Kronecker delta
777	$\dot{\boldsymbol{\epsilon}}_{plastic}$ is the plastic strain rate
778	$\dot{\boldsymbol{\epsilon}}_{elastic}$ is the elastic strain rate
779	$\lambda$ is the plastic multiplier rate
780	$g$ is the plastic potential function
781	$\dot{\boldsymbol{\epsilon}}_{total}$ is the total strain rate
782	$\dot{\boldsymbol{\epsilon}}$ is the deviatoric strain rate
783	$\nu$ is Poisson's ratio
784	$E$ is the elastic Young's Modulus
785	$G$ is the shear modulus
786	$K$ is the Bulk elastic modulus
787	$f(I_1, J_2)$ is the yield surface, or yield criterion
788	$g(I_1, J_2)$ is the plastic potential function
789	$\psi$ is the dilatancy angle
790	$I_1$ is the first stress invariant
791	$J_2$ is the second stress invariant
792	$\alpha_\phi$ is the first Ducker-Prager material constant
793	$k_c$ is the second Ducker-Prager material constant
794	$\dot{\boldsymbol{\omega}}$ is the spin rate tensor
795	$\epsilon_{v0}$ is the initial volumetric strain
796	$\epsilon_v$ is the volumetric strain
797	$c_0$ is the initial cohesion
798	$\boldsymbol{\tau}_f$ is the fluid Cauchy stress tensor
799	$P_f$ is the fluid pressure
800	$\eta_f$ is the fluids dynamic viscosity
801	$\mathcal{A}$ is the mobility of the fluid at the interface
802	$\mathcal{C}_{DG}$ is the drag coefficient
803	$U_{T,c}$ is the settling velocity of the solids, structured solids and confined fluids
804	$U_{T,uc}$ is the settling velocity of the unstructured solids
805	$\mathcal{F}$ is the drag contribution from solid-like drag
806	$\mathcal{G}$ is the drag contribution from fluid-like drag
807	$S_p$ is the smoothing function
808	$\mathcal{K}$ is the absolute total mass flux



809  $M(Re_p)$  is an empirical function weakly dependent on the Reynolds number  
 810  $\mathcal{P}$  the partitioning parameter for the fluid and solid like contributions to drag  
 811  $m$  is an exponent for  $\mathcal{P}$   
 812  $C_{VMG}$  is the virtual mass coefficient  
 813  $|\mathbf{S}|$  is the norm of the shear force  
 814  $N$  is the normal force on a plane element  
 815  $g$  is the gravitational acceleration  
 816  $P_{b,s,u}$  is the basal pressure from  
 817  $P_{b,u}$  is the basal pressure from the free fluids  
 818  $P_{b,c}$  is the basal pressure from the solids, structured solids and confined fluids  
 819  $\mathcal{B}$  is the pressure propagation factor for structured solids  
 820  $K_a$  is the active lateral earth pressure coefficient  
 821  $K_p$  is the passive lateral earth pressure coefficient  
 822  $\zeta$  is a shape factor for the vertical gradient in solid concentration  
 823  $n$  is Mannings surface roughness coefficient  
 824  $X$  is the shape factor for the vertical fluid velocity profile  
 825  $Re_p$  is the particle Reynolds Number  
 826  $N_R$  is the Reynolds Number  
 827  $N_{RA}$  is the interfacial Reynolds Number  
 828  $H$  is the typical height of the flow  
 829  $L$  is the typical length of the flow  
 830  $\alpha$  is the first viscosity parameter  
 831  $\beta$  the second viscosity parameter  
 832  $d$  is the grain diameter  
 833  $W$  is the kernel weight function  
 834  $r$  is the distance  
 835  $h$  is the kernel width (not to be confused with the flow height)  
 836  $q$  is the normalized particle distance  
 837  $\Pi_{ij}$  is an artificial viscosity term  
 838  $F_{ij}^n R_{ij}^{\alpha\beta}$  is an artificial stress term  
 839  $\epsilon_0$  is a constant parameter for the artificial stress term  
 840  $\alpha_\Pi$  and  $\beta_\Pi$  are constants in the artificial viscous force  
 841  $u_{sound}$  is the speed of sound in the material  
 842  $N(\mathbf{x})$  is the Grid-kernel function  
 843  $c_p$  is the plastic coefficient  
 844  
 845  
 846  
 847  
 848  
 849  
 850  
 851

852 **Appendix B. Stress Remapping**

853 If, either due to degradation of strength parameters, or building numerical errors, the state of the stress  
854 tensor lies beyond the yield surface, a correction must be applied. We implement the correction scheme used by  
855 Bui et al. (2008). This scheme considers two primary ways in which the stress can have an undesired state:  
856 Tension cracking, and imperfectly plastic stress.

857 **Tension Cracking**

858 In the case of tension cracking, the stress state has moved beyond the apex of the yield surface, as  
859 described by Chen & Mizuno (1990). The employed solution in this case is to re-map the stress tensor along the  
860  $I_1$  axis to be at this apex. The apex is provided by the yield function (Equation 89)

861 89.  $-\alpha_\phi I_1 + k_c < 0$

862 To solve for this condition, the non-deviatoric stress state is increased (since  $I_1 - \frac{k_c}{\alpha_\phi}$  is negative) to lie  
863 perpendicular to the apex point on the  $I_1$  axis (Equation ).

864 90.  $\bar{\sigma}^{\gamma\gamma} = r_S^{\gamma\gamma} - \frac{1}{3} \left( I_1 - \frac{k_c}{\alpha_\phi} \right)$

865 **Imperfect Plastic Stress**

866 Imperfect plastic stress described the state where the stress tensor lies above the apex, but beyond the  
867 yield criterion, thus have more stress than supported by the failure criteria that is set. This criteria is simply the  
868 yield surface itself (Equation 91).

869 91.  $-\alpha_\phi I_1 + k_c < \sqrt{J_2}$

870 For this state, re-mapping is done by scaling of the  $J_2$  value (Equations 92, 93 and 94).

871 92.  $r = \frac{-\alpha_\phi I_1 + k_c}{\sqrt{J_2}}$

872 93.  $\bar{\sigma}^{\gamma\gamma} = r_S^{\gamma\gamma} + \frac{1}{3} I_1$

873 94.  $\bar{\sigma}^{xy} = r_S^{xy}, \bar{\sigma}^{xz} = r_S^{xz}, \bar{\sigma}^{yz} = r_S^{yz}$

874

875

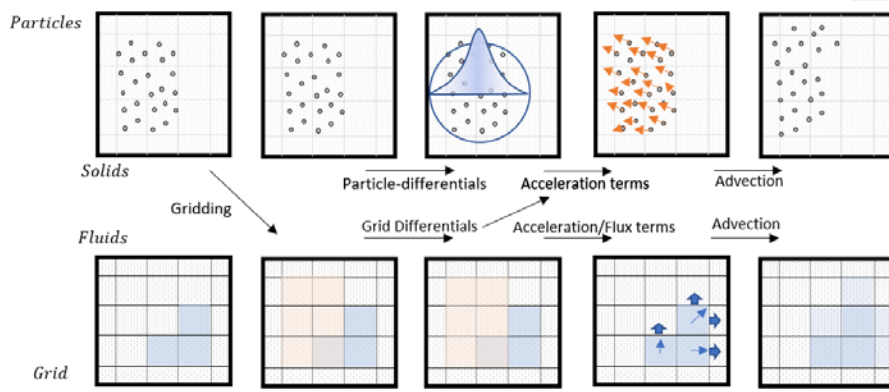
876

877 **Appendix C. Software Implementation**

878 The model presented in this article is part of the continued development of the OpenLISEM modelling  
 879 tools. The most recent set of equations of implemented in the open-source alpha version of OpenLISEM Hazard  
 880 2. Here, we describe the details of the implementation of the model into software.

881 **Hybrid MPM**

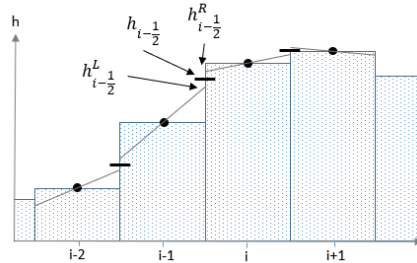
882 We utilize the MPM framework to be able to discretize part of the equations on a Eulerian regular grid,  
 883 and part of the equations on the Lagrangian particles. Our distinct take on this method is the representation of the  
 884 fluid phase completely as a finite element solution, while solids are simulated as discrete particle volumes. This  
 885 allows the model to use the major benefits that are present when depth-averaged fluid flow is simulated in a grid.  
 886 Both numerical efficiency, and high-accuracy coupling with hydrology are lacking in particle methods. For the  
 887 solid phase, non-dissipative advection, fracturing and stiffness is a major benefit of the MPM approach. Since  
 888 our model assumed confined fluids share their velocity with the solids, we advect the confined fluids as part of  
 889 the particles. Total fluid volume is then calculated from the free fluids in the finite element data, and the gridded  
 890 particle data. A flowchart of the software setup is provided in figure 6.



891  
 892 *Figure 9 The sub-steps taken by the software to complete a single step of numerical integration.*

893 **Finite element solution**

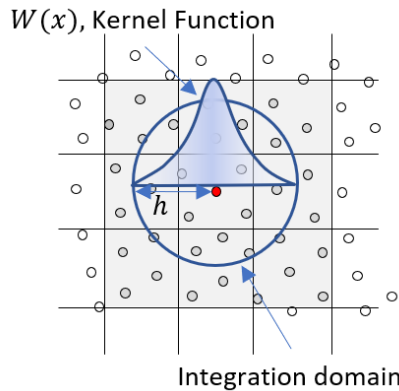
894 We use a regular cartesian grid to describe the modelling domain. Terrain and cell-boundary based  
 895 variables are re-produced using the MUSCL piecewise linear reconstruction (Delestre et al., 2014). For each cell-  
 896 boundary, a left and right estimation of acceleration terms, velocity updates and new discharges is made. The left  
 897 estimates use left-reconstructed variables while the other uses right-reconstructed variables. The final average  
 898 flux through the boundary determines actual mass and momentum transfer. Local acceleration is averaged from  
 899 the right estimate of the left boundary and left estimate of the right boundary. An additional benefit of the used  
 900 scheme is the automatic estimation of continuous and discontinuous terrain. The piecewise linear reconstructions  
 901 do not guarantee smooth terrain, for sharp locally variable terrain, pressure terms from vertical walls arise that  
 902 block momentum. These terms allow for better estimation of momentum loss by barriers, but can be turned off if  
 903 required for the simulated scenario.



904 *Figure 10 Piecewise linear reconstruction is used by the MUSCL scheme to estimate values of flow*  
 905 *heights, velocities and terrain at cell-boundaries.*

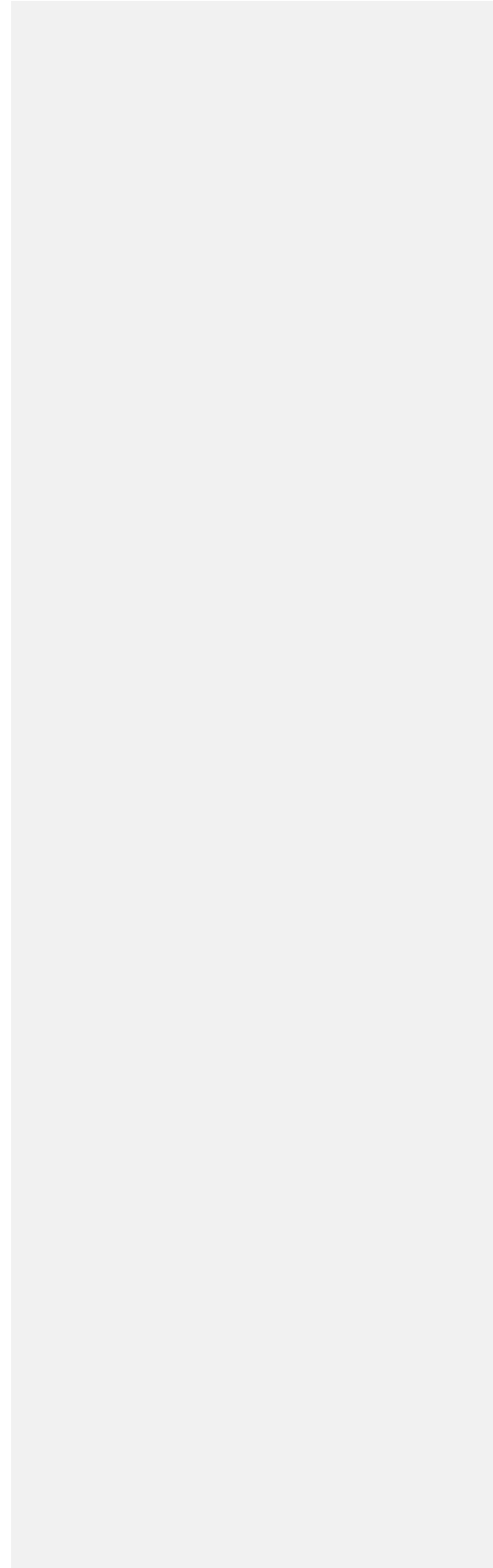
907 **GPU acceleration using OpenCL/OpenGL**

908 In order to create a more efficient setup, both the finite element and particle interactions are performed  
 909 on the GPU. We utilize the OpenCL API to compile kernels written in c-style language. These kernels are  
 910 compiled at the start of the simulation, and thereby allow for easy customization by users. While the usage of  
 911 OpenCL 1.1 forces the usage of single precision floating point numbers, it allows for a wider range of GPU types  
 912 to be supported. Finite element solutions on the GPU are straightforward, as maps are a basic data storage type  
 913 for graphical processing units. Particles are stored as single-precision floating point arrays. Within the  
 914 framework of MPM, iteration of particles within a kernel is required for each timestep and particle. This  
 915 effectively means  $O(n^2)$  operations are required. Significant efficiency improvements are obtained by pre-  
 916 calculation sorting. Particles are sorted based on their location within the finite element grid. Based on the id of  
 917 the gridcell, a bitonic mergesort is performed. This sorting algorithm works seamlessly on parallel architecture  
 918 and operates as  $O(n \log^2(n))$  (Batcher, 1968). The then, a raster is allocated to store the first indexed occurrence  
 919 within the sorted list of particles of that gridcell. Since the kernel used for the presented work extends at most to  
 920 a full width of two gridcells, we must iterate over all particles present in 9 neighboring grid cells.



921 *Figure 11 By limiting the kernel with and sorting particles before calculation, only the distance of*  
 922 *particles in neighboring cells need to be checked, significantly reducing computational load, particularly for*  
 923 *larger datasets.*

924  
 925 A final benefit to the usage of OpenCL is direct access to simulation variables for visualization in  
 926 OpenGL using the OpenGL/OpenCL interoperability functionality. The built-in viewing window of OpenLISEM  
 927 Hazard 2.0 alpha directly uses the data to draw both particles, shapefiles and grid data using customizable  
 928 shaders written in the OpenGL shader language.



930

## References

931

[Aaron, J., & Hungr, O. \(2016\). Dynamic simulation of the motion of partially-coherent landslides. \*Engineering Geology\*, 205, 1-11.](#)

932

933

Abe, K., & Konagai, K. (2016). Numerical simulation for runout process of debris flow using depth-averaged material point method. *Soils and Foundations*, 56(5), 869-888.

934

935

Alsaman, M. E., Myers, M. T., & Sharf-Aldin, M. H. (2015, November). Comparison of multistage to single stage triaxial tests. In *49th US Rock Mechanics/Geomechanics Symposium*. American Rock Mechanics Association.

936

937

938

Bandara, S., Ferrari, A., & Laloui, L. (2016). Modelling landslides in unsaturated slopes subjected to rainfall infiltration using material point method. *International Journal for Numerical and Analytical Methods in Geomechanics*, 40(9), 1358-1380.

939

940

941

Batcher, K. E. (1968, April). Sorting networks and their applications. In *Proceedings of the April 30--*

942

*May 2, 1968, spring joint computer conference* (pp. 307-314).

943

Beutner, E. C., & Gerbi, G. P. (2005). Catastrophic emplacement of the Heart Mountain block slide,

944

Wyoming and Montana, USA. *Geological Society of America Bulletin*, 117(5-6), 724-735.

945

Bieniawski, Z. T. (1967, October). Mechanism of brittle fracture of rock: part I—theory of the fracture

946

process. In *International Journal of Rock Mechanics and Mining Sciences & Geomechanics Abstracts* (Vol. 4,

947

No. 4, pp. 395-406). Pergamon.

948

Bout, B., & Jetten, V. G. (2018). The validity of flow approximations when simulating catchment-

949

integrated flash floods. *Journal of hydrology*, 556, 674-688.

950

Bui, H. H., Fukagawa, R., Sako, K., & Ohno, S. (2008). Lagrangian meshfree particles method (SPH)

951

for large deformation and failure flows of geomaterial using elastic-plastic soil constitutive model. *International*

952

*journal for numerical and analytical methods in geomechanics*, 32(12), 1537-1570.

953

Chen, W. F., & Mizuno, E. (1990). *Nonlinear analysis in soil mechanics* (No. BOOK). Amsterdam:

954

Elsevier.

955

Cohen, D., Lehmann, P., & Or, D. (2009). Fiber bundle model for multiscale modeling of

956

hydromechanical triggering of shallow landslides. *Water resources research*, 45(10).

957

Corominas, J., Matas, G., & Ruiz-Carulla, R. (2019). Quantitative analysis of risk from fragmental

958

rockfalls. *Landslides*, 16(1), 5-21.

959

Corominas, J., van Westen, C., Frattini, P., Cascini, L., Malet, J. P., Fotopoulou, S., ... & Pitilakis, K.

960

(2014). Recommendations for the quantitative analysis of landslide risk. *Bulletin of engineering geology and the*

961

*environment*, 73(2), 209-263.

962

[Cuomo, S., Pastor, M., Capobianco, V., & Cascini, L. \(2016\). Modelling the space-time evolution of](#)

963

[bed entrainment for flow-like landslides. \*Engineering geology\*, 212, 10-20.](#)

964

DAVID, L. G., & RICHARD, M. (2011). A two-phase debris-flow model that includes coupled

965

evolution of volume fractions, granular dilatancy, and pore-fluid pressure. *Italian journal of engineering geology*

966

*and Environment*, 43, 415-424.

967

Davies, T. R., & McSaveney, M. J. (2009). The role of rock fragmentation in the motion of large

968

landslides. *Engineering Geology*, 109(1-2), 67-79.

969

Davies, T. R., McSaveney, M. J., & Beetham, R. D. (2006). Rapid block glides: slide-surface

970

fragmentation in New Zealand's Waikaremoana landslide. *Quarterly Journal of Engineering Geology and*

971

*Hydrogeology*, 39(2), 115-129.

972

De Vuyst, T., & Vignjevic, R. (2013). Total Lagrangian SPH modelling of necking and fracture in

973

electromagnetically driven rings. *International Journal of Fracture*, 180(1), 53-70.

974

Delaney, K. B., & Evans, S. G. (2014). The 1997 Mount Munday landslide (British Columbia) and the

975

behaviour of rock avalanches on glacier surfaces. *Landslides*, 11(6), 1019-1036.

976

Delestre, O., Cordier, S., Darboux, F., Du, M., James, F., Laguerre, C., ... & Planchon, O. (2014).

977

FullSWOF: A software for overland flow simulation. In *Advances in hydroinformatics* (pp. 221-231). Springer,

978

Singapore.

Formatted: Font: (Default) Times New Roman, English (United States)

Formatted: Font: (Default) Times New Roman

979 Dhanmeher, S. (2017). Crack pattern observations to finite element simulation: An exploratory study  
980 for detailed assessment of reinforced concrete structures.

981 Drew, D. A. (1983). Mathematical modeling of two-phase flow. *Annual review of fluid*  
982 *mechanics*, 15(1), 261-291.

983 Dufresne, A., Geertsema, M., Shugar, D. H., Koppes, M., Higman, B., Haeussler, P. J., ... & Gulick, S.  
984 P. S. (2018). Sedimentology and geomorphology of a large tsunamigenic landslide, Taan Fiord,  
985 Alaska. *Sedimentary Geology*, 364, 302-318.

986 Evans, S. G., Mugnozza, G. S., Strom, A. L., Hermanns, R. L., Ischuk, A., & Vinnichenko, S. (2006).  
987 Landslides from massive rock slope failure and associated phenomena. In *Landslides from massive rock slope*  
988 *failure* (pp. 03-52). Springer, Dordrecht.

989 Fornes, P., Bihs, H., Thakur, V. K. S., & Nordal, S. (2017). Implementation of non-Newtonian rheology  
990 for Debris Flow simulation with REEF3D. IAHR World Congress.

991 Grady, D. E., & Kipp, M. E. (1980, June). Continuum modelling of explosive fracture in oil shale.  
992 In *International Journal of Rock Mechanics and Mining Sciences & Geomechanics Abstracts* (Vol. 17, No. 3,  
993 pp. 147-157). Pergamon.

994 [Greco, M., Di Cristo, C., Iervolino, M., & Vacca, A. \(2019\). Numerical simulation of mud-flows](#)  
995 [impacting structures. \*Journal of Mountain Science\*, 16\(2\), 364-382.](#)

996 Griffiths, D. V., & Lane, P. A. (1999). Slope stability analysis by finite elements. *Geotechnique*, 49(3),  
997 387-403.

998 Hayir, A. (2003). The effects of variable speeds of a submarine block slide on near-field tsunami  
999 amplitudes. *Ocean engineering*, 30(18), 2329-2342.

1000 Hušek, M., Kala, J., Hokeš, F., & Král, P. (2016). Influence of SPH regularity and parameters in  
1001 dynamic fracture phenomena. *Procedia engineering*, 161, 489-496.

1002 Hutter, K., Svendsen, B., & Rickenmann, D. (1994). Debris flow modeling: A review. *Continuum*  
1003 *mechanics and thermodynamics*, 8(1), 1-35.

1004 Ishii, M. (1975). Thermo-fluid dynamic theory of two-phase flow. *NASA Sti/recon Technical Report*  
1005 *A*, 75.

1006 Ishii, M., & Zuber, N. (1979). Drag coefficient and relative velocity in bubbly, droplet or particulate  
1007 flows. *AIChE journal*, 25(5), 843-855.

1008 Iverson, R. M. (2012). Elementary theory of bed-sediment entrainment by debris flows and  
1009 avalanches. *Journal of Geophysical Research: Earth Surface*, 117(F3).

1010 Iverson, R. M., & Denlinger, R. P. (2001). Flow of variably fluidized granular masses across three-  
1011 dimensional terrain: 1. Coulomb mixture theory. *Journal of Geophysical Research: Solid Earth*, 106(B1), 537-  
1012 552.

1013 Iverson, R. M., & Denlinger, R. P. (2001). Flow of variably fluidized granular masses across three-  
1014 dimensional terrain: 1. Coulomb mixture theory. *Journal of Geophysical Research: Solid Earth*, 106(B1), 537-  
1015 552.

1016 Iverson, R. M., & George, D. L. (2014). A depth-averaged debris-flow model that includes the effects  
1017 of evolving dilatancy. I. Physical basis. *Proceedings of the Royal Society A: Mathematical, Physical and*  
1018 *Engineering Sciences*, 470(2170), 20130819.

1019 Iverson, R. M., & Ouyang, C. (2015). Entrainment of bed material by Earth-surface mass flows: Review  
1020 and reformulation of depth-integrated theory. *Reviews of Geophysics*, 53(1), 27-58.

1021 Jakob, M., Hungr, O., & Jakob, D. M. (2005). *Debris-flow hazards and related phenomena* (Vol. 739).  
1022 Berlin: Springer.

1023 Kaklauskas, G., & Ghaboussi, J. (2001). Stress-strain relations for cracked tensile concrete from RC  
1024 beam tests. *Journal of Structural Engineering*, 127(1), 64-73.

1025 Kern, J. S. (1995). Evaluation of soil water retention models based on basic soil physical properties. *Soil*  
1026 *Science Society of America Journal*, 59(4), 1134-1141.

Formatted: Font: (Default) Times New Roman, English (United States)

- 1027 Kjekstad, O., & Highland, L. (2009). Economic and social impacts of landslides. In *Landslides—disaster*  
1028 *risk reduction* (pp. 573-587). Springer, Berlin, Heidelberg.
- 1029 Li, C., Wang, C., & Qin, H. (2015). Novel adaptive SPH with geometric subdivision for brittle fracture  
1030 animation of anisotropic materials. *The Visual Computer*, 31(6-8), 937-946.
- 1031 Libersky, L. D., & Petschek, A. G. (1991). Smooth particle hydrodynamics with strength of materials.  
1032 In *Advances in the free-Lagrange method including contributions on adaptive gridding and the smooth particle*  
1033 *hydrodynamics method* (pp. 248-257). Springer, Berlin, Heidelberg.
- 1034 Loehnert, S., & Mueller-Hoeppe, D. S. (2008). Multiscale methods for fracturing solids. In *IUTAM*  
1035 *symposium on theoretical, computational and modelling aspects of inelastic media* (pp. 79-87). Springer,  
1036 Dordrecht.
- 1037 Luna, B. Q., Remaître, A., Van Asch, T. W., Malet, J. P., & Van Westen, C. J. (2012). Analysis of  
1038 debris flow behavior with a one dimensional run-out model incorporating entrainment. *Engineering*  
1039 *geology*, 128, 63-75.
- 1040 Ma, G. W., Wang, Q. S., Yi, X. W., & Wang, X. J. (2014). A modified SPH method for dynamic failure  
1041 simulation of heterogeneous material. *Mathematical Problems in Engineering*, 2014.
- 1042 Matsui, T., & San, K. C. (1992). Finite element slope stability analysis by shear strength reduction  
1043 technique. *Soils and foundations*, 32(1), 59-70.
- 1044 Maurel, B., & Combesure, A. (2008). An SPH shell formulation for plasticity and fracture analysis in  
1045 explicit dynamics. *International journal for numerical methods in engineering*, 76(7), 949-971.
- 1046 Menin, R. G., Trautwein, L. M., & Bittencourt, T. N. (2009). Smeared crack models for reinforced  
1047 concrete beams by finite element method. *RIEM-IBRACON Structures and Materials Journal*, 2(2).
- 1048 [Mergili, M., Frank, B., Fischer, J. T., Huggel, C., & Pudasaini, S. P. \(2018\). Computational experiments](#)  
1049 [on the 1962 and 1970 landslide events at Huascarán \(Peru\) with r. avafLOW: Lessons learned for predictive mass](#)  
1050 [flow simulations. \*Geomorphology\*, 322, 15-28.](#)
- 1051 Monaghan, J. J. (2000). SPH without a tensile instability. *Journal of computational physics*, 159(2),  
1052 290-311.
- 1053 Nadim, F., Kjekstad, O., Peduzzi, P., Herold, C., & Jaedicke, C. (2006). Global landslide and avalanche  
1054 hotspots. *Landslides*, 3(2), 159-173.
- 1055 Necas, J., & Hlaváček, I. (2017). *Mathematical theory of elastic and elasto-plastic bodies: an*  
1056 *introduction*. Elsevier.
- 1057 Ngekpe, B. E., Ode, T., & Eluozo, S. N. (2016). Application of total-strain crack model in finite  
1058 element analysis for punching shear at edge connection. *International journal of Research in Engineering and*  
1059 *Social Sciences*, 6(12), 1-9.
- 1060 O'brien, J. S. (2007). FLO-2D users manual. *Nutr. Ariz. June*.
- 1061 O'brien, J. S., & Julien, P. Y. (1985). Physical properties and mechanics of hyperconcentrated sediment  
1062 flows. *Proc. ASCE HD Delineation of landslides, flash flood and debris flow Hazards*.
- 1063 Osorno, M., & Steeb, H. (2017). Coupled SPH and Phase Field method for hydraulic  
1064 fracturing. *PAMM*, 17(1), 533-534.
- 1065 Pailha, M., & Pouliquen, O. (2009). A two-phase flow description of the initiation of underwater  
1066 granular avalanches. *Journal of Fluid Mechanics*, 633, 115-135.
- 1067 Pastor, M., Blanc, T., Haddad, B., Petrone, S., Morles, M. S., Drempetic, V., ... & Cuomo, S. (2014).  
1068 Application of a SPH depth-integrated model to landslide run-out analysis. *Landslides*, 11(5), 793-812.
- 1069 Pastor, M., Blanc, T., Pastor, M. J., Sanchez, M., Haddad, B., Mira, P., ... & Drempetic, V. (2007). A  
1070 SPH depth integrated model with pore pressure coupling for fast landslides and related phenomena. In *2007*  
1071 *international forum on landslides disaster management* (pp. 987-1014).
- 1072 Pastor, M., Haddad, B., Sorbino, G., Cuomo, S., & Drempetic, V. (2009). A depth-integrated, coupled  
1073 SPH model for flow-like landslides and related phenomena. *International Journal for numerical and analytical*  
1074 *methods in geomechanics*, 33(2), 143-172.

Formatted: Font: (Default) Times New Roman, English (United States)

Formatted: Font: (Default) Times New Roman



1075 Pitman, E. B., & Le, L. (2005). A two-fluid model for avalanche and debris flows. *Philosophical*  
1076 *Transactions of the Royal Society A: Mathematical, Physical and Engineering Sciences*, 363(1832), 1573-1601.

1077 Price, N. J. (2016). *Fault and joint development: in brittle and semi-brittle rock*. Elsevier.

1078 Pudasaini, S. P. (2012). A general two-phase debris flow model. *Journal of Geophysical Research:*  
1079 *Earth Surface*, 117(F3).

1080 Pudasaini, S. P., & Fischer, J. T. (2016). A mechanical erosion model for two-phase mass flows. *arXiv*  
1081 *preprint arXiv:1610.01806*.

1082 Pudasaini, S. P., & Hutter, K. (2003). Rapid shear flows of dry granular masses down curved and  
1083 twisted channels. *Journal of Fluid Mechanics*, 495, 193-208.

1084 Pudasaini, S. P., & Hutter, K. (2007). *Avalanche dynamics: dynamics of rapid flows of dense granular*  
1085 *avalanches*. Springer Science & Business Media.

1086 Pudasaini, S. P., & Mergili, M. (2019). A Multi-Phase Mass Flow Model. *Journal of Geophysical*  
1087 *Research: Earth Surface*.

1088 Pudasaini, S. P., Hajra, S. G., Kandel, S., & Khattri, K. B. (2018). Analytical solutions to a nonlinear  
1089 diffusion–advection equation. *Zeitschrift für angewandte Mathematik und Physik*, 69(6), 150.

1090 Reiche, P. (1937). The Toreva-Block: A distinctive landslide type. *The Journal of Geology*, 45(5), 538-  
1091 548. Richard, A., Brennan, G., Oh, W. T., & Ileme, V. (2017). Critical height of an unsupported vertical trench in  
1092 an unsaturated sand. In *Proceedings of the 70th Canadian Geotechnical Conference*.

1093 Rickenmann, D., Laigle, D. M. B. W., McArdell, B. W., & Hübl, J. (2006). Comparison of 2D debris-  
1094 flow simulation models with field events. *Computational Geosciences*, 10(2), 241-264.

1095 Roberts, M., <http://extremelearning.com.au/evenly-distributing-points-in-a-triangle/> Obtained 29-01-  
1096 2020

1097 Savage, S. B., & Hutter, K. (1989). The motion of a finite mass of granular material down a rough  
1098 incline. *Journal of fluid mechanics*, 199, 177-215.

1099 Saxton, K. E., & Rawls, W. J. (2006). Soil water characteristic estimates by texture and organic matter  
1100 for hydrologic solutions. *Soil science society of America Journal*, 70(5), 1569-1578.

1101 Sheridan, M. F., Stinton, A. J., Patra, A., Pitman, E. B., Bauer, A., & Nichita, C. C. (2005). Evaluating  
1102 Titan2D mass-flow model using the 1963 Little Tahoma peak avalanches, Mount Rainier, Washington. *Journal*  
1103 *of Volcanology and Geothermal Research*, 139(1-2), 89-102.

1104 Stead, D., & Wolter, A. (2015). A critical review of rock slope failure mechanisms: The importance of  
1105 structural geology. *Journal of Structural Geology*, 74, 1-23.

1106 Steffen, M., Kirby, R. M., & Berzins, M. (2008). Analysis and reduction of quadrature errors in the  
1107 material point method (MPM). *International journal for numerical methods in engineering*, 76(6), 922-948.

1108 Sticko, S. (2013). Smooth Particle Hydrodynamics applied to fracture mechanics.

1109 Stomakhin, A., Schroeder, C., Chai, L., Teran, J., & Selle, A. (2013). A material point method for snow  
1110 simulation. *ACM Transactions on Graphics (TOG)*, 32(4), 1-10.

1111 Tang, C. L., Hu, J. C., Lin, M. L., Angelier, J., Lu, C. Y., Chan, Y. C., & Chu, H. T. (2009). The  
1112 Tsaoling landslide triggered by the Chi-Chi earthquake, Taiwan: insights from a discrete element  
1113 simulation. *Engineering Geology*, 106(1-2), 1-19.

1114 Van Asch, T. W., Tang, C., Alkema, D., Zhu, J., & Zhou, W. (2014). An integrated model to assess  
1115 critical rainfall thresholds for run-out distances of debris flows. *Natural hazards*, 70(1), 299-311.

1116 Van Looy, K., Bouma, J., Herbst, M., Koestel, J., Minasny, B., Mishra, U., ... & Schaap, M. G. (2017).  
1117 Pedotransfer functions in Earth system science: Challenges and perspectives. *Reviews of Geophysics*, 55(4),  
1118 1199-1256.

1119 Varnes, D. J. (1978). Slope movement types and processes. *Special report*, 176, 11-33.

1120 von Boetticher, A., Turowski, J. M., McArdell, B. W., Rickenmann, D., & Kirchner, J. W. (2016).  
1121 DebrisInterMixing-2.3: a finite volume solver for three-dimensional debris-flow simulations with two calibration  
1122 parameters-Part I: Model description. *Geoscientific Model Development*, 9(9), 2909-2923.

- 1123 Williams, J. R. (2019, October). Application of SPH to coupled fluid-solid problems in the petroleum  
1124 industry. In *Videos of Plenary Lectures presented at the IV International Conference on Particle-Based*  
1125 *Methods. Fundamentals and Applications.(PARTICLES 2015)*.
- 1126 Xie, M., Esaki, T., & Cai, M. (2006). GIS-based implementation of three-dimensional limit equilibrium  
1127 approach of slope stability. *Journal of geotechnical and geoenvironmental engineering*, 132(5), 656-660.
- 1128 Xu, F., Zhao, Y., Li, Y., & Kikuchi, M. (2010). Study of numerical and physical fracture with SPH  
1129 method. *Acta Mechanica Solida Sinica*, 23(1), 49-56.
- 1130 Zhang, L. L., Zhang, J., Zhang, L. M., & Tang, W. H. (2011). Stability analysis of rainfall-induced  
1131 slope failure: a review. *Proceedings of the Institution of Civil Engineers-Geotechnical Engineering*, 164(5), 299-  
1132 316.
- 1133 Zhou, F., Molinari, J. F., & Ramesh, K. T. (2005). A cohesive model based fragmentation analysis:  
1134 effects of strain rate and initial defects distribution. *International Journal of Solids and Structures*, 42(18-19),  
1135 5181-5207.